Validating a Density-Profiling System for Asphalt Compaction Assessment

PUBLICATION NO. FHWA-HRT-24-143

AUGUST 2024

U.S. Department of Transportation
Federal Highway Administration

Research, Development, and Technology
Turner-Fairbank Highway Research Center
6300 Georgetown Pike
McLean, VA 22101-2296

FOREWORD

Proper asphalt compaction is crucial because it directly influences the long-term durability of roadway pavements. Without adequate compaction, asphalt surfaces can quickly degrade, leading to potholes, cracks, and other forms of deterioration that pose hazards to drivers and increase maintenance costs.

This interim report documents an extensive investigation undertaken to independently evaluate and validate a nondestructive testing technology for asphalt compaction assessment known as the density-profiling system (DPS). The investigation tests the sensitivity of DPS to various temperature and moisture conditions, explores the fundamental mechanisms of using DPS in the laboratory and in the field, and documents lessons learned from a field trial. The findings of this investigation contribute to the broader body of knowledge in pavement technology, highlighting how innovative tools can enhance construction practices.

The outcomes of this study provide valuable insights that assist pavement owners in comprehending DPS technology and its application in the assessment of asphalt compaction. Civil engineers, construction managers, and policymakers will find the information particularly beneficial as they seek to adopt more advanced and effective methods for infrastructure development and maintenance. Additionally, researchers and academics in the field of transportation engineering can leverage the detailed analysis presented here to further explore and refine nondestructive testing techniques for asphalt pavements. This report is also useful for industry stakeholders and equipment manufacturers aiming to improve product offerings and better meet the demands of modern roadway construction and upkeep.

Jean Nehme, P.E., Ph.D.
Director, Office of Infrastructure
Research and Development

Notice

This document is disseminated under the sponsorship of the U.S. Department of Transportation (USDOT) in the interest of information exchange. The U.S. Government assumes no liability for the use of the information contained in this document.

Non-Binding Contents

Except for the statutes and regulations cited, the contents of this document do not have the force and effect of law and are not meant to bind the States or the public in any way. This document is intended only to provide information regarding existing requirements under the law or agency policies.

Quality Assurance Statement

The Federal Highway Administration (FHWA) provides high-quality information to serve Government, industry, and the public in a manner that promotes public understanding. Standards and policies are used to ensure and maximize the quality, objectivity, utility, and integrity of its information. FHWA periodically reviews quality issues and adjusts its programs and processes to ensure continuous quality improvement.

Disclaimer for Product Names and Manufacturers

The U.S. Government does not endorse products or manufacturers. Trademarks or manufacturers' names appear in this document only because they are considered essential to the objective of the document. They are included for informational purposes only and are not intended to reflect a preference, approval, or endorsement of any one product or entity.

Recommended citation: Federal Highway Administration, *Validating a Density-Profiling System for Asphalt Compaction Assessment* (Washington, DC: 2024) https://doi.org/10.21949/1521588.

TECHNICAL REPORT DOCUMENTATION PAGE

1. Report No. FHWA-HRT-24-143	2. Government Accession No.	3. Recipient's Catalog No.
4. Title and Subtitle Validating a Density-Profiling System for Asphalt Compaction Assessment		5. Report Date August 2024
		6. Performing Organization Code
7. Author(s) Hoda Azari (ORCID: 0000-0002-7340-0035) Heng Liu (ORCID: 0000-0001-5746-1279)		8. Performing Organization Report No.
9. Performing Organization Name and Address Highway Technology Partners LLC 9220 Rumsey Road, Suite 100 Columbia, MD 21045		10. Work Unit No.
		11. Contract or Grant No.
12. Sponsoring Agency Name and Address Office of Infrastructure Research and Development Federal Highway Administration 6300 Georgetown Pike McLean, VA 22101-2296		13. Type of Report and Period Covered October 2019–July 2023
		14. Sponsoring Agency Code HRDI-20
15. Supplementary Notes The contracting officer's representative was Hoda Azari (HRDI-20).		

16. Abstract

Highway agencies are demonstrating significant interest in enhancing the quality assurance of asphalt pavement compaction by initiating the Transportation Pooled Fund project TPF-5(443). This pooled fund explores a nondestructive testing technology known as the density-profiling system (DPS). Currently, compaction assessment relies on field coring, which is invasive and time-consuming, or nuclear gauges, which offer spot evaluations of paving surfaces. However, the DPS uses air-coupled, ground-penetrating radar to provide continuous measurements for compaction assessment, which promises quicker data acquisition and broader coverage of paving surfaces. DPS technology holds great potential for advancing the current practice of compaction assessment for hot mix asphalt (HMA) pavements. In collaboration with the Transportation Pooled Fund Program project TPF-5(443), the FHWA's Nondestructive Evaluation Program independently evaluates and validates DPS technology. This study examines the impact of temperature and moisture on DPS measurements. Furthermore, this study conducts an analytical investigation to understand the scanning boundary of DPS measurements. The analytical results demonstrated that DPS measurements are sensitive to a thin layer beneath the pavement surface. The report also documents how the edge effect affects measurements when DPS is used on laboratory HMA samples. The findings confirm the presence of measurement errors attributed to the edge effect. Consequently, the study proposes practical solutions to effectively mitigate these errors. Additionally, this study evaluates various models to correlate dielectric measurements obtained by DPS to the density information of laboratory HMA samples and finds that the linear regression fits the laboratory data well. Lastly, this report shares experiences and lessons learned from a field implementation of DPS for a paving project in Greenbelt, MD.

17. Key Words Density-profiling system, asphalt, nondestructive evaluation, ground-penetrating radar	18. Distribution Statement No restrictions. This document is available to the public through the National Technical Information Service, Springfield, VA 22161. https://www.ntis.gov

19. Security Classif. (of this report) Unclassified	20. Security Classif. (of this page) Unclassified	21. No. of Pages 65	22. Price N/A

SI* (MODERN METRIC) CONVERSION FACTORS

APPROXIMATE CONVERSIONS TO SI UNITS

Symbol	When You Know	Multiply By	To Find	Symbol
		LENGTH		
in	inches	25.4	millimeters	mm
ft	feet	0.305	meters	m
yd	yards	0.914	meters	m
mi	miles	1.61	kilometers	km
		AREA		
in^2	square inches	645.2	square millimeters	mm^2
ft^2	square feet	0.093	square meters	m^2
yd^2	square yard	0.836	square meters	m^2
ac	acres	0.405	hectares	ha
mi^2	square miles	2.59	square kilometers	km^2
		VOLUME		
fl oz	fluid ounces	29.57	milliliters	mL
gal	gallons	3.785	liters	L
ft^3	cubic feet	0.028	cubic meters	m^3
yd^3	cubic yards	0.765	cubic meters	m^3
	NOTE: volumes greater than 1,000 L shall be shown in m^3			
		MASS		
oz	ounces	28.35	grams	g
lb	pounds	0.454	kilograms	kg
T	short tons (2,000 lb)	0.907	megagrams (or "metric ton")	Mg (or "t")
		TEMPERATURE (exact degrees)		
°F	Fahrenheit	5 (F-32)/9 or (F-32)/1.8	Celsius	°C
		ILLUMINATION		
fc	foot-candles	10.76	lux	lx
fl	foot-Lamberts	3.426	$candela/m^2$	cd/m^2
		FORCE and PRESSURE or STRESS		
lbf	poundforce	4.45	newtons	N
lbf/in^2	poundforce per square inch	6.89	kilopascals	kPa

APPROXIMATE CONVERSIONS FROM SI UNITS

Symbol	When You Know	Multiply By	To Find	Symbol
		LENGTH		
mm	millimeters	0.039	inches	in
m	meters	3.28	feet	ft
m	meters	1.09	yards	yd
km	kilometers	0.621	miles	mi
		AREA		
mm^2	square millimeters	0.0016	square inches	in^2
m^2	square meters	10.764	square feet	ft^2
m^2	square meters	1.195	square yards	yd^2
ha	hectares	2.47	acres	ac
km^2	square kilometers	0.386	square miles	mi^2
		VOLUME		
mL	milliliters	0.034	fluid ounces	fl oz
L	liters	0.264	gallons	gal
m^3	cubic meters	35.314	cubic feet	ft^3
m^3	cubic meters	1.307	cubic yards	yd^3
		MASS		
g	grams	0.035	ounces	oz
kg	kilograms	2.202	pounds	lb
Mg (or "t")	megagrams (or "metric ton")	1.103	short tons (2,000 lb)	T
		TEMPERATURE (exact degrees)		
°C	Celsius	1.8C+32	Fahrenheit	°F
		ILLUMINATION		
lx	lux	0.0929	foot-candles	fc
cd/m^2	candela/m2	0.2919	foot-Lamberts	fl
		FORCE and PRESSURE or STRESS		
N	newtons	2.225	poundforce	lbf
kPa	kilopascals	0.145	poundforce per square inch	lbf/in^2

*SI is the symbol for International System of Units. Appropriate rounding should be made to comply with Section 4 of ASTM E380. (Revised March 2003)

TABLE OF CONTENTS

LIST OF FIGURES

LIST OF TABLES

LIST OF ABBREVIATIONS AND SYMBOLS

Abbreviations

AASHTO	American Association of State Highway and Transportation Officials
AC	air-void content
AIC	Akaike information criterion
AMPT	asphalt mixture performance tester
DPS	density-profiling system
EM	electromagnetic
FDTD	finite-difference time domain
FHWA	Federal Highway Administration
GPR	ground-penetrating radar
HMA	hot mix asphalt
MnDOT	Minnesota Department of Transportation
NDE	nondestructive evaluation
NDT	nondestructive testing
ODOT	Ohio Department of Transportation
RDM	rolling density meter
RMSE	root-mean-square error
Rx	receiver
SGC	Superpave gyratory compacted
SSE	sum of squared errors
Tx	transmitter

Variables

A	signal amplitude
a	antenna separation distance
AC	air-void content
AC_i	AC at the *i*th testing point
A_i	incident wave
A_r	reflected wave
c	speed of light
D	travel distance
D_{s1}	distance from transmitter to particle
D_{s2}	distance from particle to receiver
D_{surf}	two-way travel distance
f	center frequency
H	antenna height
R	sample radius
t	time
ε	dielectric constant

CHAPTER 1. INTRODUCTION

Highway agencies show strong interest in advancing quality assurance of asphalt pavement compaction by setting up a Transportation Pooled Fund project TPF-5(443) to investigate density-profiling systems (DPSs) (MnDOT 2024a). The current practice in compaction assessment relies on either field coring processes or nuclear gauges, which provide spot assessment of paving surfaces. DPS uses air-coupled, ground-penetrating radar (GPR) to collect continuous measurements for compaction assessment, aiming to provide faster data acquisition for a wide coverage of paving surfaces. DPS technology shows promise in advancing the current practice for compaction assessment of hot-mix asphalt (HMA) pavements.

As part of the pooled fund project, the Federal Highway Administration (FHWA) Nondestructive Evaluation (NDE) Program at Turner-Fairbank Highway Research Center provides technical assistance for understanding, evaluating, and validating DPS technology regarding the compaction assessment of asphalt pavements. This report synthesizes research contributed by the NDE Program.

Chapter 2 reports on equipment tests of the environmental effects (i.e., temperature and moisture) on the DPS measurements. The preliminary results motivated later DPS research activities.

Chapter 3 provides an analytical study to understand the fundamentals of DPS technology regarding one of the dielectric measurement methods: the surface reflection method. The study reveals an analytical model that can calculate the method's scanning boundary. The resulting scanning boundary shows that by means of the surface reflection method, the DPS may be sensitive only to a thin layer underneath the pavement surface.

Chapter 4 documents a study on the edge effect of using DPS for laboratory measurement of cylindrical HMA samples. The study uses numerical simulations and experimental testing to confirm the existence of the edge effect in testing cylindrical HMA samples. The study provides practical suggestions to mitigate the edge effect.

Chapter 5 presents a study in evaluating the modeling process for correlation of dielectric measurements obtained by DPS to the density information of HMA pavements. The study evaluates various models' performance in developing the relationship.

Chapter 6 shares fieldwork experiences and lessons learned from the NDE Program for DPS use in a paving project in Greenbelt, MD. The work is to validate the protocols and guidelines of the use of DPS in field measurements.

CHAPTER 2. EQUIPMENT TESTING

INTRODUCTION

Equipment testing aimed to explore how environmental factors and pavement conditions affect the dielectric constant of HMA (ε_{HMA}). Experimental studies have been designed to explore the influence of various environmental factors, such as temperature and moisture, on the ε_{HMA}. Additionally, testing and studies investigated how the sample size of SGC samples affects the ε.

The study included laboratory testing of SGC samples under controlled environmental conditions, as well as field measurements on actual pavements. Understanding the relationship between environmental effects, pavement compaction, and ε_{HMA} can contribute to the development of more accurate models and predictive tools for assessing pavement conditions, evaluating performance, and optimizing maintenance strategies. On the other hand, according to the Minnesota Department of Transportation's (MnDOT) experience, a bias is usually present between the correlation curves developed using SGC samples versus the ones generated using field cores. While differences in field-testing and laboratory-testing methods and the presence of edge effects in laboratory specimens significantly contribute to the bias between cores and laboratory correlation curves, this chapter investigates environmental effects, including moisture and temperature, in causing the bias mentioned earlier.

INVESTIGATING THE ROLE OF TEMPERATURE ON DIELECTRIC MEASUREMENTS

The preliminary objective was to examine the influence of temperature on dielectric measurements of HMA specimens using DPS. To achieve the objective, the study used a temperature-controlled chamber to manipulate the temperatures experienced by the specimens and the DPS device. The use of the chamber enabled researchers to investigate the effects of different temperature levels on the materials and their dielectric behavior.

Figure 1 shows a temperature chamber capable of accommodating both the HMA specimens and the DPS device. The chamber was equipped with precise temperature regulation capabilities, ensuring that specific temperature conditions could be achieved and maintained consistently throughout the experimental process. The ability to accommodate both the HMA specimens and the DPS device in the same chamber allowed for simultaneous testing and direct comparison of their responses to temperature variations.

This preliminary study served as a foundation for further investigations into the relationship between temperature, HMA characteristics, and DPS performance in assessment of dielectric properties. The preliminary nature of this study suggests that additional research and analysis are necessary to draw more comprehensive conclusions about the effects of temperature on HMA specimens and the DPS.

Source: FHWA.

Figure 1. Photo. Temperature-controlled environmental chamber accommodates HMA specimens and the DPS (FHWA 2024).

HMA samples were exposed to a temperature of 130 °F (54 °C) for 2 h. The DPS was kept outside the chamber during the test to avoid exposure to high temperatures. The correlation curve obtained under two temperatures revealed a shift in the correlation curve, indicating an increase in dielectric values at 130 °F (54 °C) compared with laboratory temperature. That shift suggests that the dielectric properties of the HMA samples were influenced by the elevated temperature, resulting in higher dielectric values (figure 2). However, the maximum observed change in dielectric properties from specimens was recorded as an approximately 0.075 increase from lab temperature to 130 °F (54 °C). The amount of change in the dielectric was within the American Association of State Highway and Transportation Officials (AASHTO) PP 98 requirement of 0.08 (AASHTO 2019).

As temperatures rise, the mobility of polar molecules also increases, resulting in an increase in the ε. However, when a sample of asphalt is heated to 360 °F (182 °C) or higher, the change in dielectric becomes irreversible, leading to a decrease in its value. That irreversible process can be attributed to the evaporation of certain binder compounds.

The HMA samples were then subjected to a temperature of 100 °F (38 °C) for 3 h, while the DPS was exposed to the same temperature for 30 min inside the temperature chamber. During the exposure, the dielectric properties of the samples were measured, while both the DPS and the samples remained inside the controlled-temperature chamber.

The correlation curve obtained under two temperatures is shown in figure 2, indicating a decrease in dielectric values at 100 °F (38 °C) compared with laboratory temperature. The maximum observed change in dielectric properties was recorded as an approximately 0.07 decrease from lab temperature, to 100 °F (38 °C). The decrease in the dielectric of the HMA was unexpected, while both specimens and the antenna were exposed to elevated temperatures.

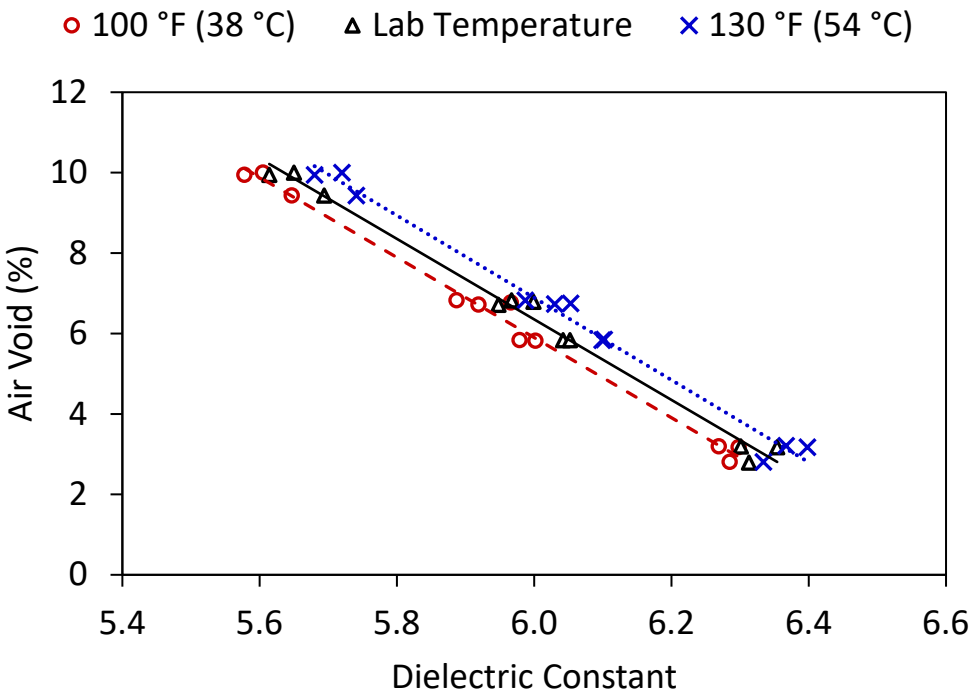

Source: FHWA.
Note: Trend equations: 100 °F (38 °C) $y = -9.9642x + 65.684$, $R^2 = 0.9917$; Lab temperature y = $-10.012x + 66.422$, $R^2 = 0.9904$; 130 °F (54 °C) $y = -10.228x + 68.257$, $R^2 = 0.9904$

Figure 2. Graph. Influence of temperature on the correlation between ε's and AC of HMA samples.

INVESTIGATING THE EFFECT OF THE SIZE AND AIR VOID UNIFORMITY OF HMA SPECIMENS

The experiments aimed to investigate the effect of the size of SGC samples on developing correlation curves. The correlation curves were generated using SGC samples and respective core samples that were directly cored off from the SGC samples.

The SGC samples were prepared according to the standardized procedure outlined in R83 (AASHTO 2022). The diameter of SGC samples were 6-inch (152.4 mm) and the diameter of core samples were 4-inch (101.6 mm), as shown in figure 3.

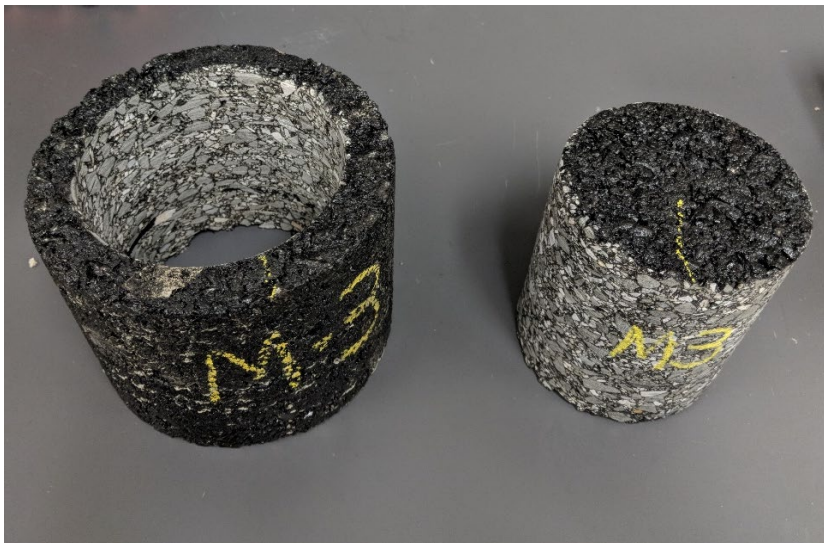

Source: FHWA.

Figure 3. Photo. Core taken from a 6-inch (152.4 mm)-diameter SGC sample.

The air voids of the cores were measured following ASTM D6752 and AASHTO T331. Correlation curves were generated using both the original SGC samples and the cores. The curves are compared in figure 4.

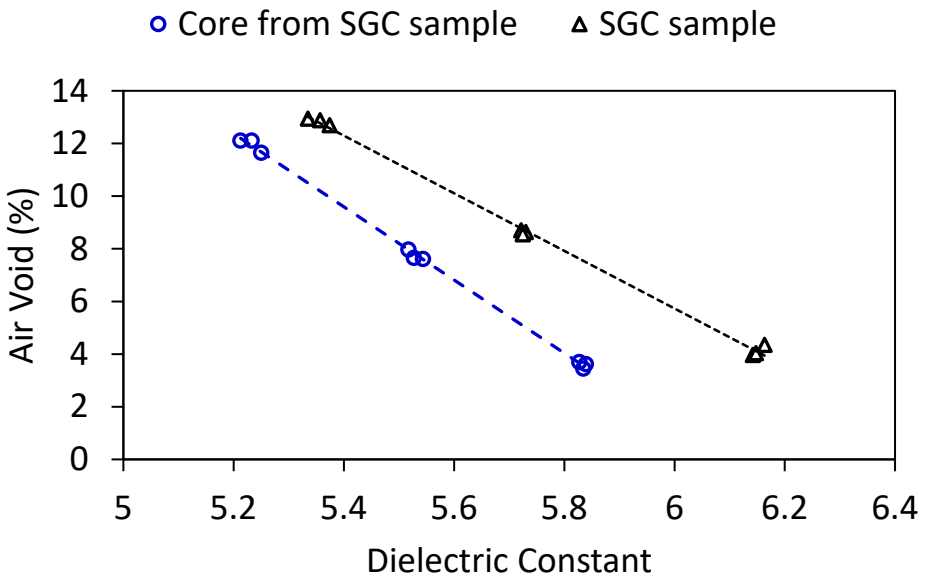

Source: FHWA.
Note: Trend equations: Core from SGC sample $y = -13.936x + 84.864$, $R^2 = 0.9991$; SGC Sample $y = -10.968x + 71.515$, $R^2 = 0.9974$.

Figure 4. Graph. Correlation curves from SGC samples and cores taken from corresponding SGC samples.

Figure 4 demonstrates a significant reduction in the ε's of the cores compared with the original specimens. While the density of the core specimens changed slightly from the original specimens due to compaction uniformity, the reduction in diameter of the cores significantly influenced the dielectric measurements, which was likely due to edge refractions affecting the dielectric measurement process.

Moreover, the correlation curves were compared so that the dielectric values of the samples were kept the same for both the original specimens and the cores. Figure 5 highlights a bias between the two correlation curves, indicating that the air voids were slightly reduced for the cores compared with the original specimens.

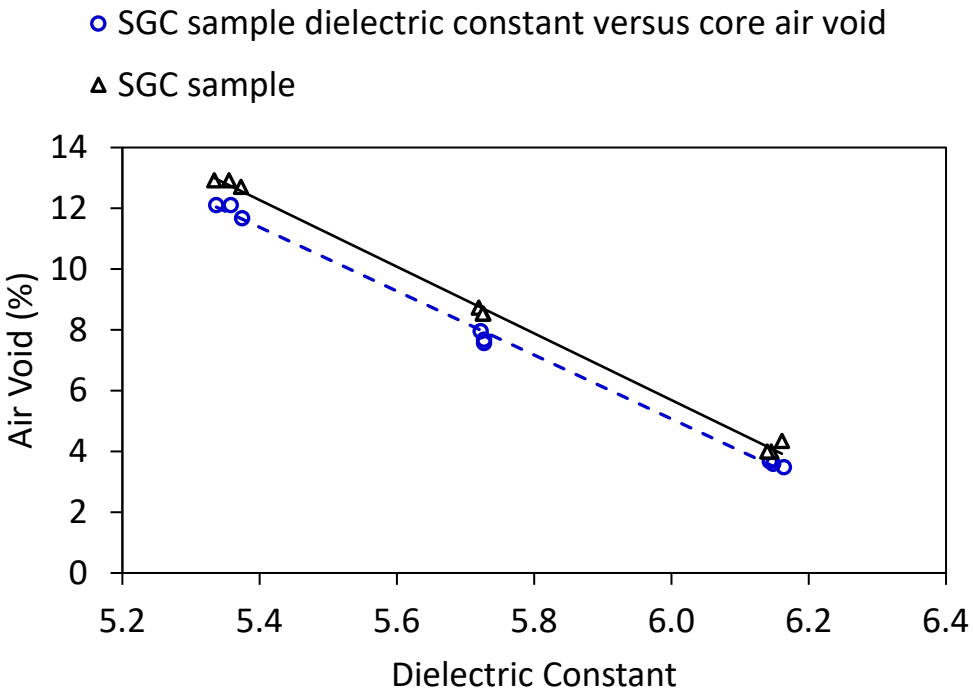

Source: FHWA.
Note: Trend equations: SGC sample ε versus core air void $y = -10.512x + 68.14$, $R^2 = 0.9968$; SGC Sample $y = -10.968x + 71.515$, $R^2 = 0.9974$.

Figure 5. Graph. Correlation curves of SGC samples and their cores.

The study findings indicate that the air voids of the cores decreased by an average of 0.48 percent at low dielectric values and 0.84 percent at mid and high dielectric values, which suggests that reducing the SGC samples to less than 6 inches in diameter is not recommended. Additionally, the study findings demonstrate that alterations in AC distribution have a minimal effect on correlation curves.

EFFECT OF MOISTURE ON DIELECTRIC MEASUREMENTS

The study delved into exploring the impact of moisture on HMA. Initial investigations assessed the effects of moisture by carefully applying water to the surfaces of the specimens. Preliminary results on laboratory samples demonstrated a noticeable increase in dielectric measurements of the HMA samples when exposed to varying amounts of water. The water application was meticulously controlled using a scale, as depicted in figure 6.

Source: FHWA.

Figure 6. Photo. Measuring the amount of sprayed water on the SGC sample.

The dielectric measurements were conducted using the laboratory testing module and accompanying kit accessories. The obtained results are displayed in figure 7.

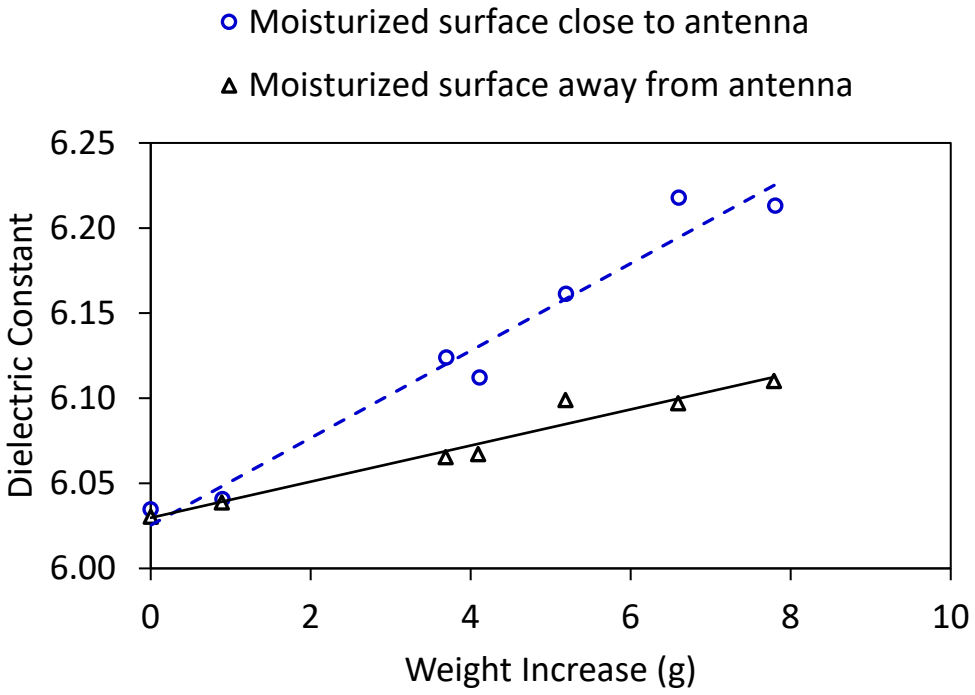

Source: FHWA.

Figure 7. Graph. Increase in ε's of the SGC samples with the increased amount of sprayed water.

The obtained results showed an increase in moisture led to higher dielectric measurements, consistent with the higher ε of water compared with the asphalt material. The experiment then advanced to field testing. Figure 8 displays the results of dielectric measurements on water-sprayed spots with 0.07 oz (2 g), 0.14 oz (4 g), 0.21 oz (6 g), 0.28 oz (8 g), and 0.35 oz (10 g) of water. The average antenna temperature recorded during the measurements was approximately 122 °F (50 °C). Table 1 presents the average ε measured by each sensor.

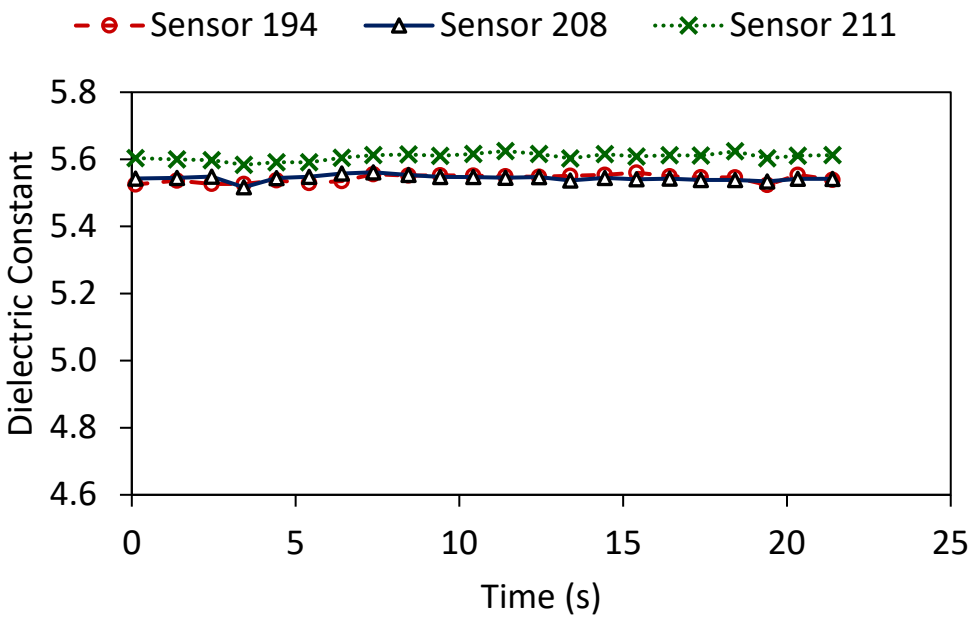

A. No water added.

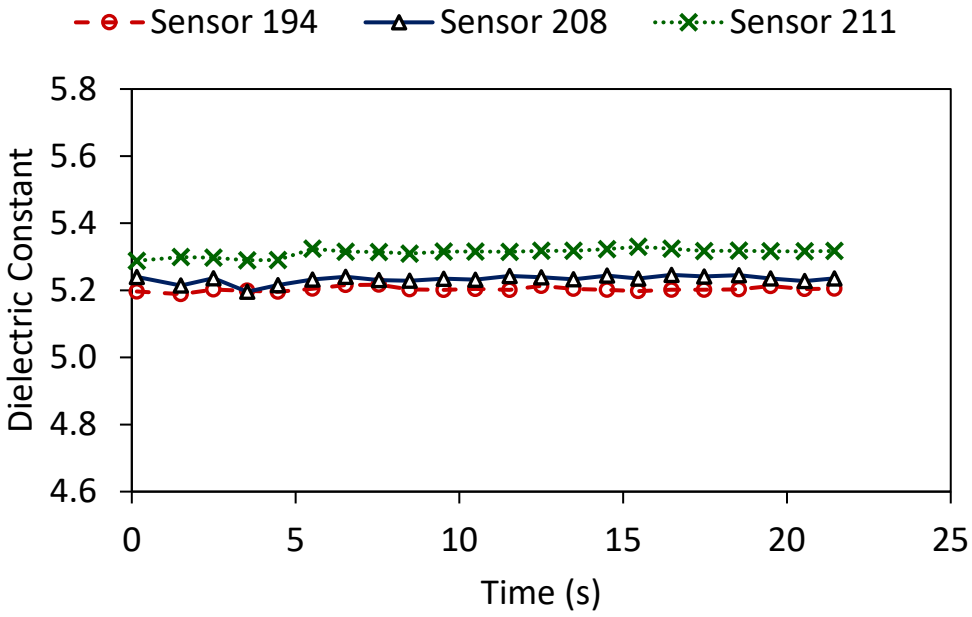

B. 0.07 oz (2 g) water added.

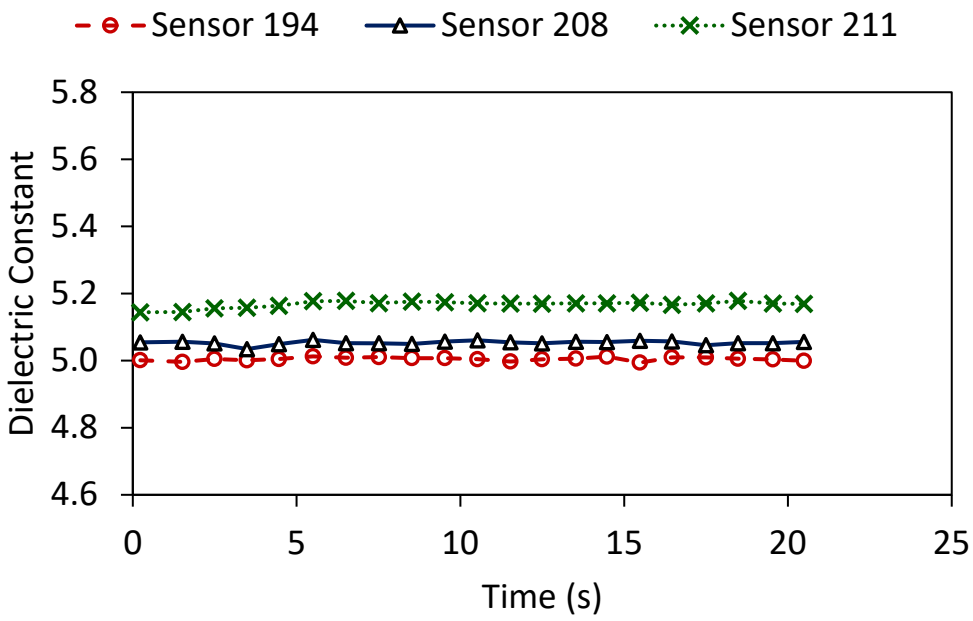

C. 0.14 oz (4 g) water added.

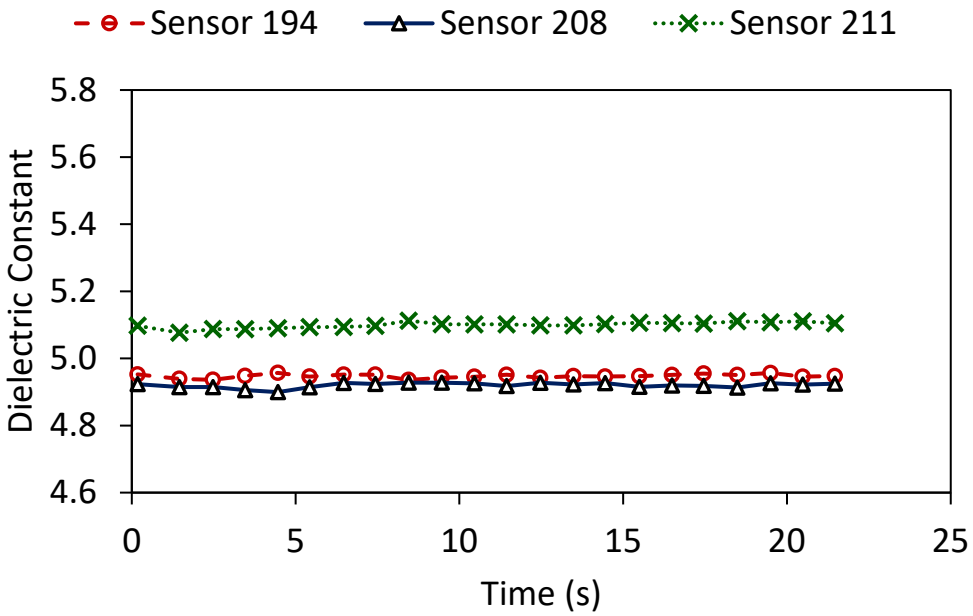

D. 0.21 oz (6 g) water added.

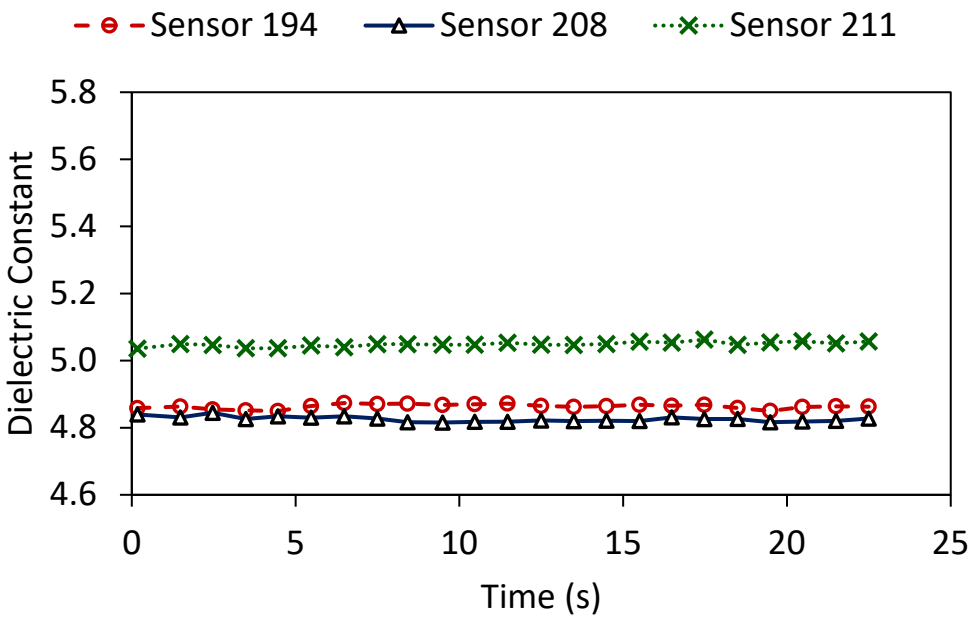

E. 0.28 oz (8 g) water added.

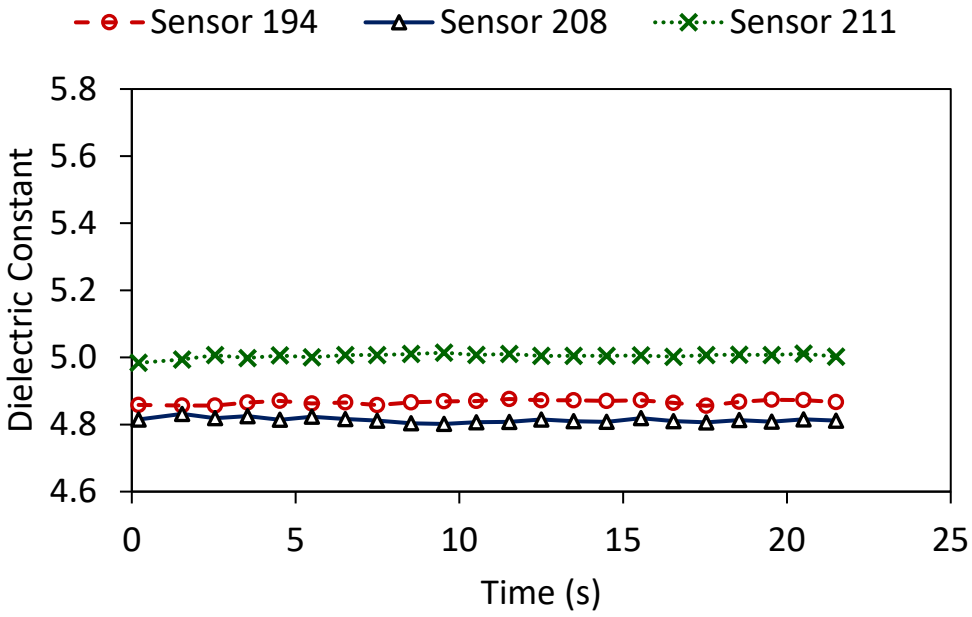

F. 0.35 oz (10 g) water added.

All images source: FHWA.

Figure 8. Graphs. Recorded ε of the same spot in *t* under different amounts of sprayed water.

Table 1. Average ε measured by each sensor.

Water Quantity (g)	Sensor 194 (Average ε)	Sensor 208 (Average ε)	Sensor 211 (Average ε)
0	5.54	5.55	5.61
2	5.20	5.24	5.31
4	5.01	5.06	5.17
6	4.95	4.93	5.10
8	4.86	4.83	5.05
10	4.86	4.81	5.00

Figure 9 provides a visual representation of the intriguing trend of decreasing ε regarding the increasing amount of sprayed water. While the HMA is hot (freshly paved HMA), the observed reduction of dielectric with moisture was unexpected, which implies that as the amount of water increased, the ε of the HMA decreased, contrary to conventional assumptions.

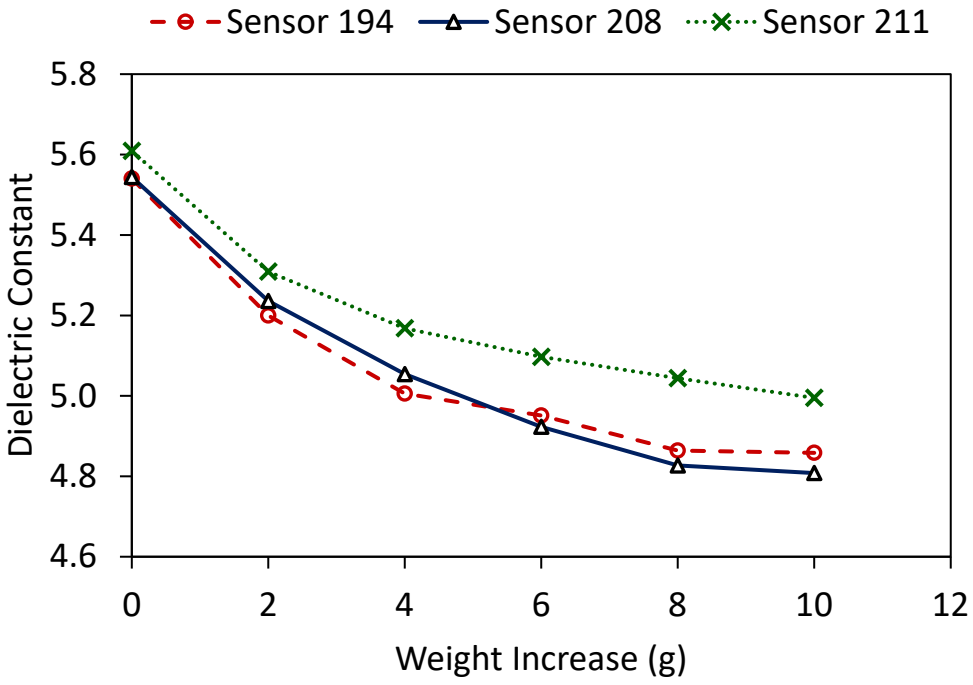

Source: FHWA.
Note: 1 g = 0.03 oz.

Figure 9. Graph. Decrease in ε of the asphalt with the increased amount of sprayed water on a freshly paved HMA pavement.

The area where water was sprayed underwent examination by infrared camera, as shown in figure 10 temperatures compared with the surrounding areas, with a maximum temperature reduction of approximately 81 °F (27 °C).

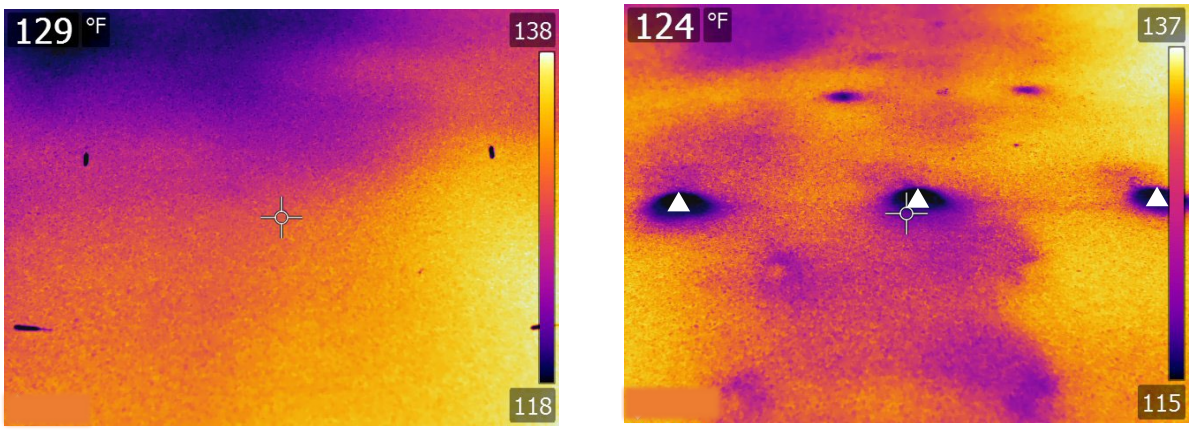

A. Before spraying water.

B. After spraying water. A triangle marker indicates the water-sprayed area.

All images source: FHWA.

Figure 10. Photos. Temperature dropped after spraying water on the HMA pavement.

The unexpected results may be due to the closed pores' inhibiting the water from penetrating through the asphalt mix (Fernandes, Fernandes, and Pais 2017). To test that assumption, an additional experimental test was performed on an existing pavement, in which the closed porosity may become reopened due to distress. The study performed the tests in the *t* mode and collected the data. The system recorded the sensor temperature at about 82.4 °F (28 °C). Figure 11 shows the results obtained from sensor 211.

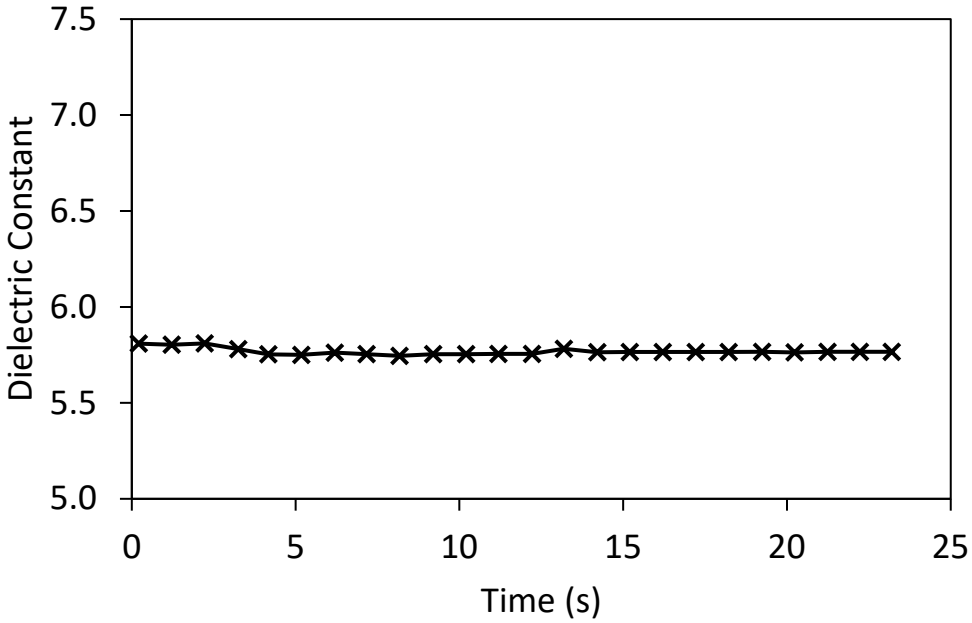

A. No water added.

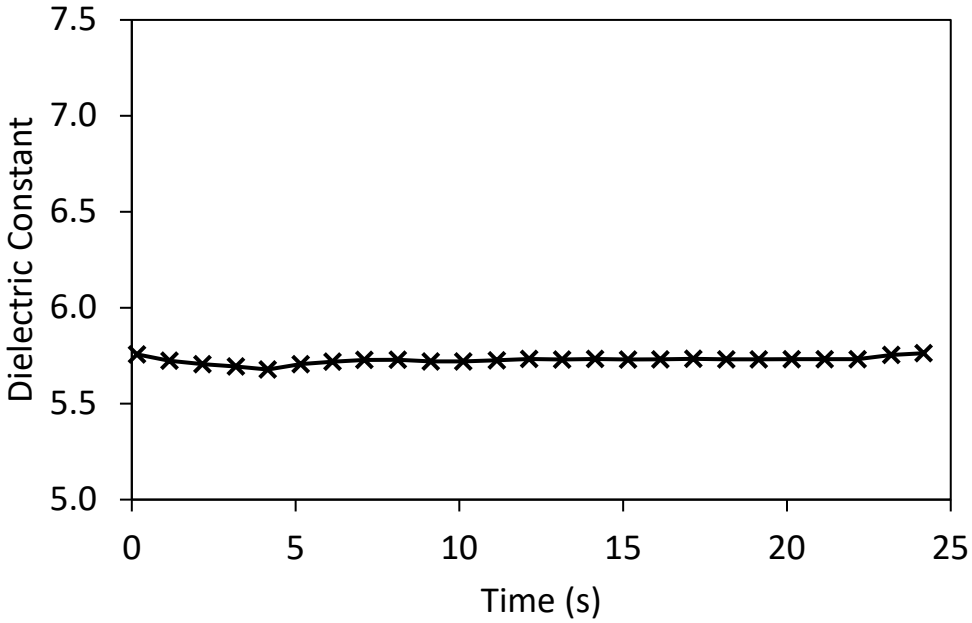

B. 0.07 oz (2 g) water added.

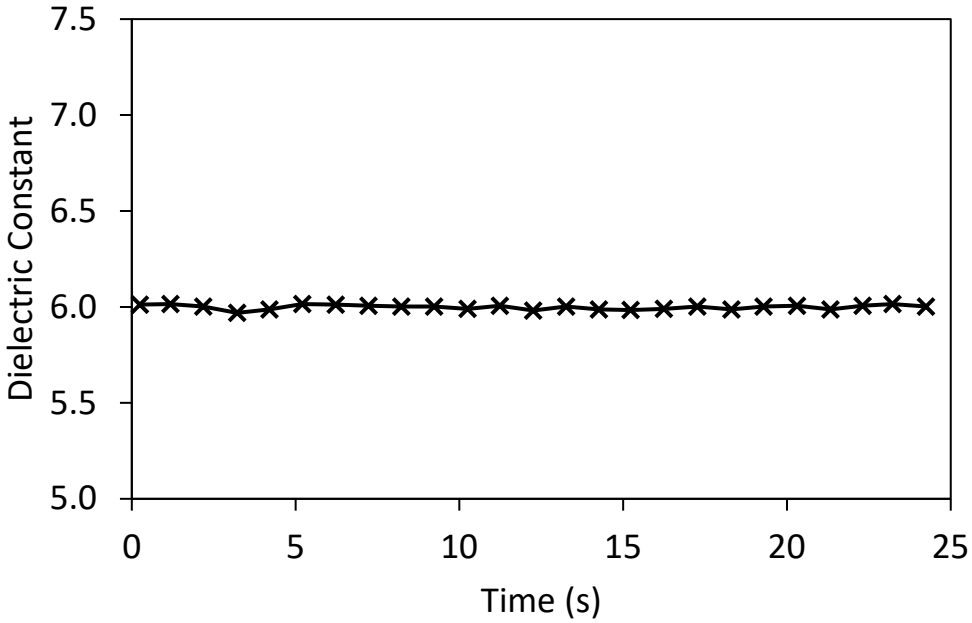

C. 0.14 oz (4 g) water added.

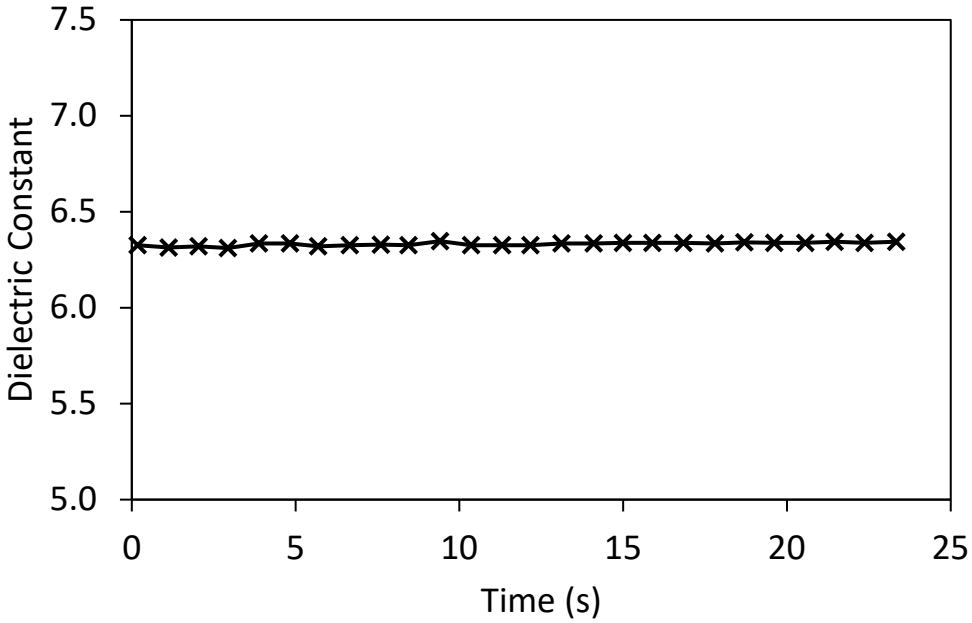

D. 0.21 oz (6 g) water added.

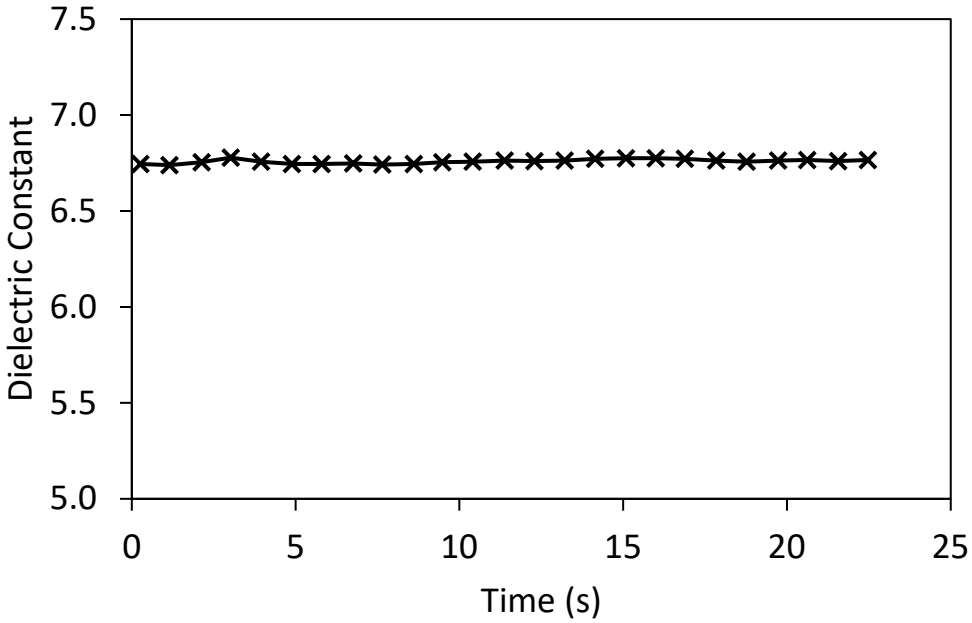

E. 0.28 oz (8 g) water added.

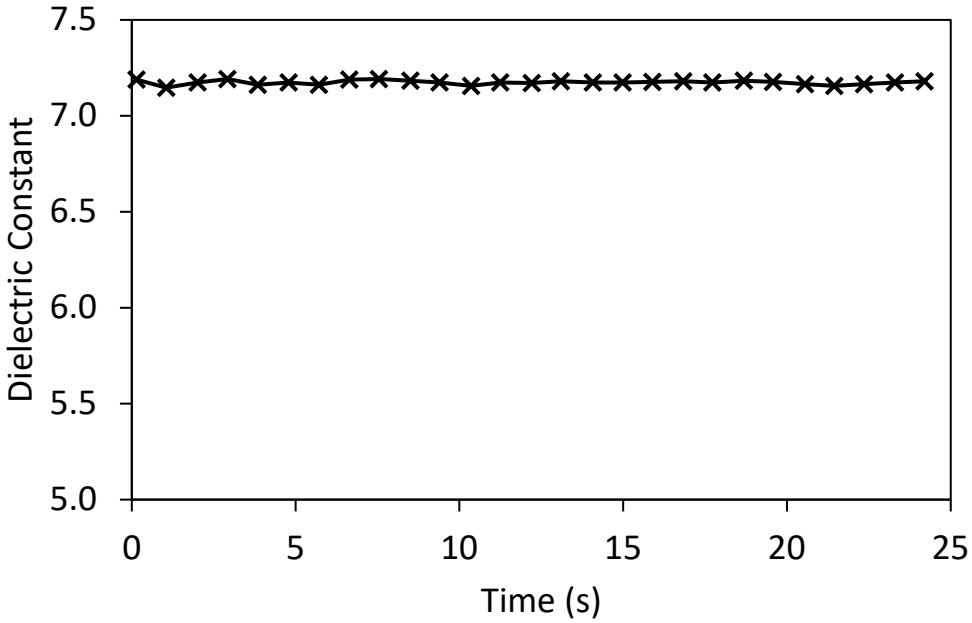

F. 0.35 oz (10 g) water added.

All images source: FHWA.

Figure 11. Graphs. Results of dielectric measurement with varying water application on an old pavement, based on sensor 211.

The dielectric measurements have been averaged and are presented in figure 12. As expected, figure 12 illustrates a clear, increasing trend in the average ε with the amount of sprayed water. The trend aligns with the higher ε of water compared with asphalt materials, confirming our initial expectations.

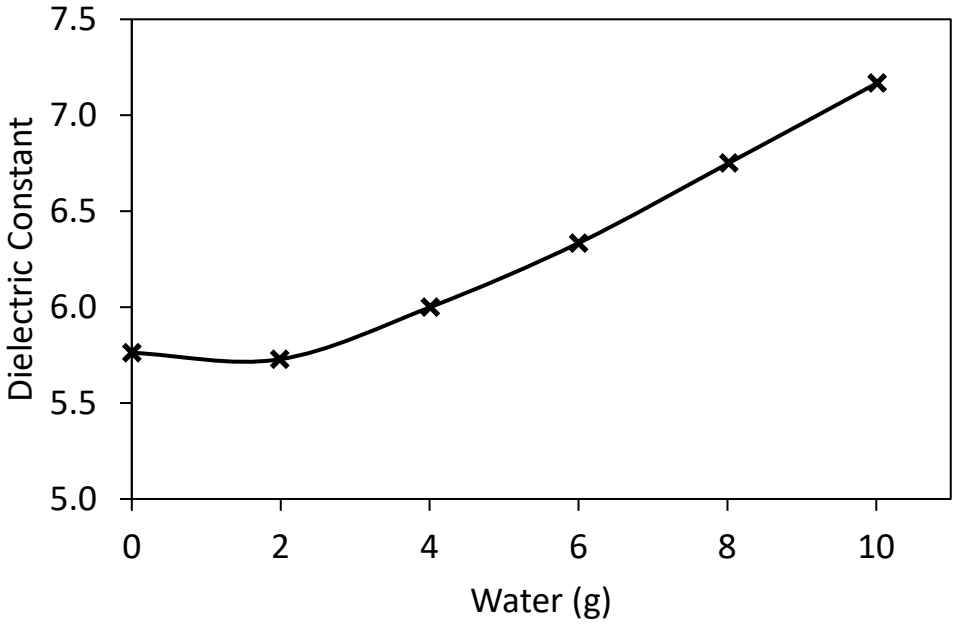

Source: FHWA.

Figure 12. Graph. Increase in ε of asphalt with the increased amount of sprayed water on an existing pavement.

CHAPTER 3. SCANNING BOUNDARY OF THE SURFACE REFLECTION METHOD FOR DIELECTRIC PROFILING OF HMA PAVEMENTS

INTRODUCTION

The compaction of HMA is characterized by HMA's density or the percentage of AC in the material. The effects of pavement compaction have shown significant impacts on pavement functionality; an increase of 1 percent in air void above the 7-percent baseline may result in an approximately 10-percent loss in pavement service life (Linden, Mahoney, and Jackson 1989). Current practice in the measurement of pavement compaction relies on coring samples (T 166, T 311, and T 209 (AASHTO 2002, 2020, 2023)) or nuclear gauges (D2950 (ASTM 2011)) or both. Recent studies have attempted to use GPR for dielectric profiling of HMA, which measures AC by inverse calculation through correlations (Hoegh et al. 2019) or mixing models (Cao and Al-Qadi 2021). While the development of an appropriate correlation may require local density measurements, the DPS shows extra values in lieu of those classic local measurements, which can be appealing for quality assurance in pavement construction. In addition to classic local measurements mandated by quality assurance programs, such as coring and nuclear gauges, dielectric profiling using GPR is nondestructive and more efficient and produces better coverage in field surveys.

For dielectric calculation, surface reflection and time-of-flight are the two major methods. Past studies have reported inconsistent results between the two approaches (Cao and Al-Qadi 2021; Hoegh et al. 2019; Porubiaková and Komačka, 2015); the surface reflection is sensitive only to a thin layer underneath the top surface, while time-of-flight represents the average dielectric through the thickness of the HMA. For samples with large AC near the surface, the two methods may result in a 20-percent difference (Cao and Al-Qadi 2021). The noticeable inconsistency between the two methods motivated the authors to investigate fundamental aspects associated with measuring approaches. This study attempts to find the scanning boundary of the surface reflection method for dielectric profiling of HMA. Rayleigh scattering theory is first used to formulate the scanning boundary. A straight ray-path-based theoretical model is then presented to determine the scanning boundary and to identify its influencing parameters. The model provides new insights about using the surface reflection method for dielectric profiling of HMA.

SCANNING BOUNDARY DUE TO RAYLEIGH SCATTERING

The surface reflection method measures the reflection coefficient regarding the ratio of the peak amplitude of reflected waves A_r to that of incident waves A_i. For air-launching tests with normal incidents, the dielectric ε of nonmagnetic materials like HMA can be determined based on figure 13.

$$\varepsilon = \left(\frac{1 + {A_r}/{A_i}}{1 - {A_r}/{A_i}} \right)^2$$

Figure 13. Equation. Dielectric measurement using the surface reflection method.

The amplitude of incident waves can be measured by covering the HMA sample with a metal plate. Because A_i is independent of the dielectric of the HMA sample, any changes in A_r will influence the dielectric measurement.

Rayleigh scattering describes the scattering of light by small particles in the order to its wavelength (Strutt 1871). More specifically, Rayleigh scattering applies to particles with circumferences equal to or less than the wavelength of the incident wave. For a 2-GHz GPR antenna as an example, the wavelength of its EM wave is approximately 0.15 m in the air and about 0.06 m in an HMA sample with a dielectric of 6. The nominal maximum size of aggregates in HMA may be up to 0.019 m, with a circumference of approximately 0.06 m under the assumption of a perfectly round shape for the aggregate. In this example, the ratio of the particle size to the wavelength of incident waves of a 2-GHz GPR antenna falls within the range of Rayleigh scattering. Consequently, the received signal may encompass scattering from aggregates underneath the HMA surface besides the direct coupling and surface reflection. The direct coupling of GPR signals can be adequately removed by subtracting measurements in open spaces from raw measurements. However, the superposition of Rayleigh scattering with surface reflection may influence the measured peak amplitude of reflected waves and the consequent calculation of dielectric.

The scattering signal arrives later than the surface reflection. When the *t* delay is sufficiently large, the superposition of Rayleigh scattering may not change the peak amplitude of reflected waves. Such a sufficient *t* delay determines a scanning boundary that any particles outside the region will not influence the scanning results. Determination of the scanning boundary depends on the sufficiency of the *t* delay. In a low-noise environment, the arrival *t* of the peak of the surface reflection is relatively consistent. As such, the *t* from the beginning of the surface reflection wave to a reference peak is the lowest or the critical *t* delay (t_c) to satisfy the sufficiency, as illustrated in figure 14. The reference peak is usually the first positive or negative peak in the wave package. Because the first positive peak has a relatively larger amplitude, which is more resistant to noises, this study selected the first positive peak as the *t* reference.

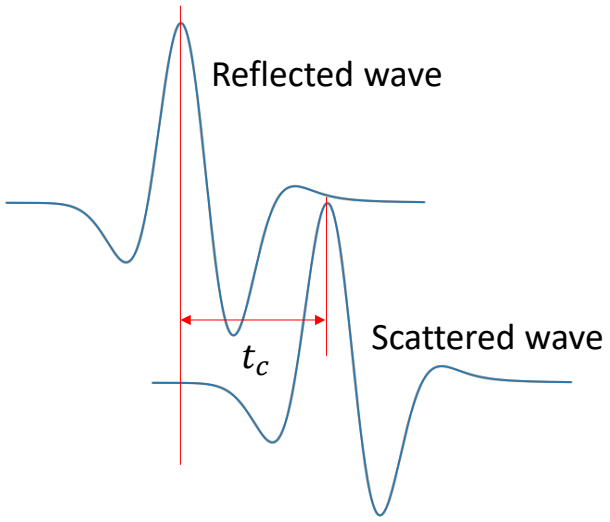

Source: FHWA.

Figure 14. Graph. Schematic illustration for critical *t* delay.

In practice, isolating the surface reflection wave from raw measurements can be cumbersome. This study proposes to use the input voltage signal of the GPR antenna to calculate the critical *t* delay. Since HMA is a nondispersive material (Saarenketo 2013), the phase of the scattering signal remains the same as the input voltage unless a phase shift occurs due to a dielectric contrast. Nonetheless, the phase shift would not change the arrival *t* of the peak but reverse the peak value from positive to negative peaks or the other way around. Figure 15 shows an identical *t* reference for the input voltage and the surface reflection. The input voltage is usually predefined by the GPR manufacturer or the user; characterizing the input voltage signal is much easier than the surface reflection wave, which requires isolation from raw measurements. For example, using the Ricker wavelet as the input voltage signal, the critical *t* delay could be $\sqrt{2}/f$, where *f* is the center frequency.

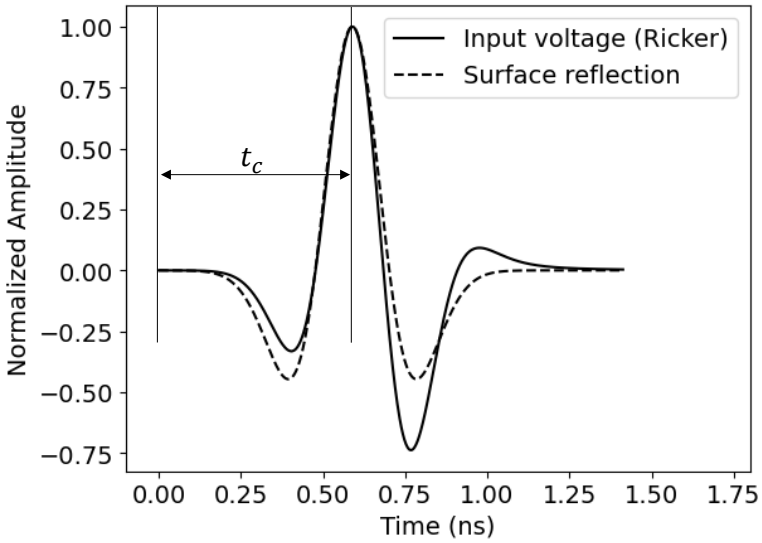

Source: FHWA.

Figure 15. Graph. Using voltage signal to determine critical *t* delay.

STRAIGHT RAY-PATH-BASED SCANNING BOUNDARY

This study uses straight ray paths to simplify the calculation without loss of generality. Figure 16 shows a two-dimensional schematic setup for dielectric profiling using air-coupled GPR with origin *O* being the surface reflection point. In figure 16, *a* is the separation distance between the Tx and Rx, *H* represents *H* to the scanning surface, ε denotes the dielectric of the background material, D_{surf} is the two-way travel distance (*D*) for the surface reflection, and D_{s1} (solid line) and D_{s2} (dashed line) are the *D's* from the Tx to the particle and from the particle to the Rx, respectively. The position of the particle is described by its coordinates (*x, y*).

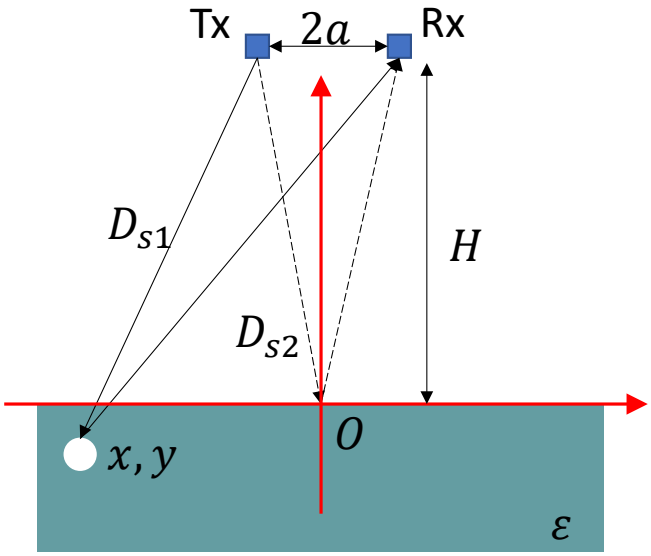

Source: FHWA.

Figure 16. Graph. Two-dimensional schematic setup for dielectric profiling using air-coupled GPR.

With the straight ray path assumption, figure 17, figure 18, and figure 19 calculate *D* of the surface reflection and the Rayleigh scattering from the particle. Figure 20 and figure 21 disclose their corresponding two-way travel *t*'s, respectively.

$$D_{surf} = 2\sqrt{a^2 + H^2}$$

Figure 17. Equation. Two-way *D* of the surface reflection.

$$D_{s1} = \sqrt{(-x - a)^2 + (H - y)^2}$$

Figure 18. Equation. One-way *D* from the transmitter to the particle.

$$D_{s2} = \sqrt{(-x + a)^2 + (H - y)^2}$$

Figure 19. Equation. One-way *D* from the particle to the *Rx*.

$$t_{surf} = \frac{D_{suf}}{c}$$

Figure 20. Equation. Two-way travel *t* of the surface reflection.

$$t_s = \frac{(D_{s1} + D_{s2}) \cdot \frac{-y}{H - y}}{c/\sqrt{\varepsilon}} + \frac{(D_{s1} + D_{s2}) \cdot \frac{H}{H - y}}{c}$$

Figure 21. Equation. Two-way travel *t* of the scattering signal.

Where c is the speed of light and $c \approx 0.3$ m/ns. Figure 22 calculates the t delay between the surface reflection and the scattering signal (t_d).

$$t_d = t_s - t_{surf}$$

Figure 22. Equation. *T* delay between the surface reflection and the scattering signal.

With a known critical t delay (e.g., $t_c = \sqrt{2}/f$ for Ricker wavelet), the scanning boundary needs to satisfy such that $t_c = t_d$.

Figure 21 indicates that for a given scanning material, the scanning boundary depends on the antenna setup, including its input voltage signal (critical t delay), separation distance, and H to the scanning surface. This study explores the sensitivity of the scanning region to the choices of center frequency and the setup of H, which are the two major parameters in field surveys.

Figure 23 shows the theoretical boundary obtained for a given GPR antenna setup at a fixed height of 3.94 ft (1.2 m), which has a separation distance of 0.013 ft (0.004 m) and uses the Ricker wavelet as input voltage with varied center frequency from 0.4 GHz to 2 GHz. The results indicate that the scanning boundary is sensitive to the choice of center frequency, and accordingly, the region becomes wider and deeper, with a larger center frequency for a fixed scanning height.

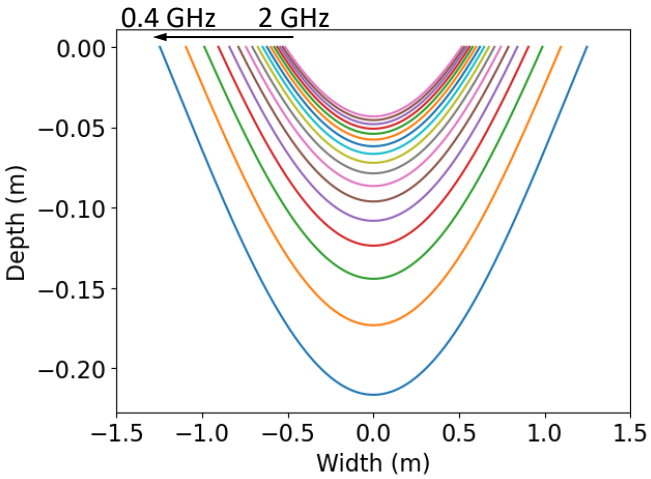

Source: FHWA.

Figure 23. Graph. Straight ray path-based scanning boundary: fixed *H* with varied center frequency from 0.4 to 2 GHz.

Figure 24 shows the theoretical boundary for the same type of GPR antenna, with a center frequency of 0.4 GHz but at a different height: from 1.31 to 6.56 ft, or 0.4 to 2 m. Similar results can be obtained for other center frequencies. The scanning boundary is also sensitive to choices of *H*'s. The region on the side becomes narrower with a lower *H*; however, the scanning depth at the center is not sensitive to the varied *H*.

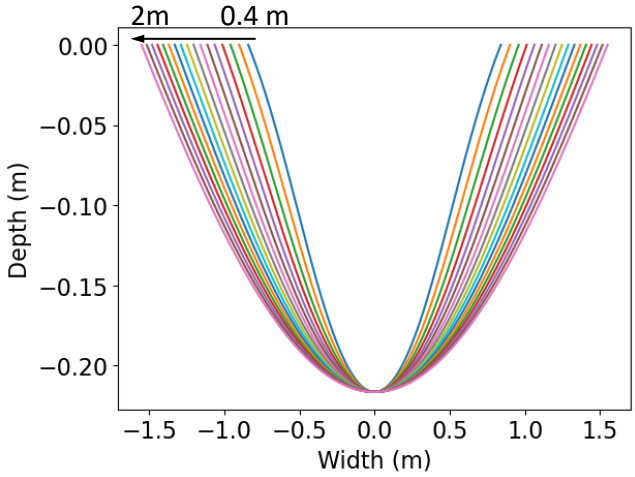

Source: FHWA.

Figure 24. Graph. Straight ray-path-based scanning boundary: fixed center frequency at 0.4 GHz with varied *H* from 1.31 to 6.56 ft, or 0.4 to 2 m.

REMARKS

This study attempts to find the scanning boundary of the surface reflection method for dielectric profiling of HMA. The study finds that Rayleigh scattering from aggregates underneath the surface will superimpose with the surface reflection wave when the wavelength of a GPR signal in HMA is in an order similar to the size of aggregate particles. The superposition may change the results of dielectric measurements using the surface reflection method. A sufficient *t* delay between the scattering signal and the surface reflection wave is required to avoid changes in the peak amplitude of reflected waves due to Rayleigh scattering. Such *t* delay formulates a scanning region such that any particles outside the region will not change the peak value of the surface reflection wave and the consequent calculation of dielectric using the surface reflection method. A straight ray-path-based theoretical model is presented to calculate the scanning boundary and to identify its influencing parameters. The model shows that the scanning boundary is sensitive to the antenna setup, including center frequency, separation distance, and *H*.

CHAPTER 4. EDGE EFFECT IN DIELECTRIC PROFILING OF CYLINDRICAL HMA SPECIMENS USING TIME-OF-FLIGHT METHOD

INTRODUCTION

The compaction of HMA pavement is characterized by its density or the percentage of AC within compacted HMA. Proper compaction of asphalt pavements necessarily ensures long-term pavement performance (Aschenbrener and Tran 2020). Current practice in measuring pavement compaction or density relies on field cores (T 166 (ASSHTO 2002)) and/or nuclear gauges (D2950 (ASTM)), both of which provide spot assessment of less than 1 percent of placed pavement. In addition, transporting and operating nuclear gauges in the United States requires a special license to ensure no radiation hazard to public health and the environment (EPA 2023a). In rare cases, damage to nuclear gauge equipment may add additional regulatory burden and environmental impacts that pavement owners would do well to consider. In recent years, GPR has emerged as an alternative NDE technique for density profiling of HMA pavements by offering advances in efficiency and coverage of data collection. Field studies by the MnDOT showed that density profiling using GPR could offer multiple orders of magnitude measurements per mile of HMA pavements (Hoegh et al. 2020).

GPR measures the bulk ε_{HMA} pavements and uses the dielectric information to calculate the pavements' densities through correlations between dielectric and AC. Due to the heterogeneous nature of asphalt material, correlation between the bulk ε and the percentage of AC within compacted HMA is a complex and active research topic. The bulk ε of heterogeneous materials was found to be well approximated by EM mixing models, such as the complex refractive index model, the Rayleigh mixing model, and the Al-Qadi-Lahouar-Leng model (Nelson 2005; Sihvola 1989; Leng 2011). These mixing models provide theoretical insights into critical factors that influence the bulk dielectric of HMA, such as types of aggregates in the HMA mixture. However, the dielectric properties of aggregates were not well reported in the literature until a few recent studies (EPA 2023b; Sias and Dave 2023). Hence, backcalculation from bulk dielectric of field cores was often used to obtain dielectric properties of aggregates (Cao and Al-Qadi 2021). Lack of sufficient data creates difficulties in the use of mixing models for field implementation, which may be alleviated partially by developing empirical correlation models from field cores or gyratory samples (Pellinen et al. 2015; Rashidi and Azari 2022; Steiner et al. 2020; Wilson and Sebesta 2015). Both mixing and empirical correlation models require accurate measurements of bulk dielectric properties of HMA specimens.

Surface reflection and time-of-flight (or two-way travel t) are the primary methods for dielectric measurements of pavements. The surface reflection method measures reflection coefficients by comparing the amplitudes of incident and reflected waves. The Fresnel equation relates the bulk ε of the scanned HMA specimen to the reflection coefficient (PP 98 (AASHTO 2019)). On the other hand, the time-of-flight method measures the bulk dielectric property by analyzing the velocity of EM waves traveling within the scanned HMA specimen (D6432 (ASTM 2019)). Unlike the surface reflection method, the time-of-flight method requires known thickness information to accurately calculate wave velocity. However, the time-of-flight method has been reported in the literature to yield relatively more robust results (Cao and Al-Qadi 2021; Hoegh et al. 2019). Laboratory testing of field cores and gyratory samples can properly measure sample

thickness by using a height gauge or a vernier caliper. Current laboratory testing uses the time-of-flight method, with small, dipole-type antennas for dielectric measurements (Hoegh et al. 2019; Sias and Dave 2023).

SGC samples are cylindrical specimens with cylinder heights of approximately 4.5 inches (approximately 11.5 cm) and a limited diameter of up to 6 inches (approximately 15 cm). Due to the limited sizes of testing samples, the challenges in laboratory testing using air-launched GPR are twofold: one is that the arrival of the direct coupling between *Tx* and *Rx* may easily interfere with surface reflection from the testing sample, and the other is that the diameter of the testing sample is much smaller than the GPR footprint. Separating the direct coupling from the surface reflection typically requires elevation of *H*, but at the same time, the GPR footprint will expand and may exceed the size of the sample surface. Both issues were corrected by coupling the GPR antenna with a known dielectric spacer (e.g., acetal homopolymer) to slow down enough the speed of EM waves, simultaneously delaying the arrival of the surface reflection from the direct coupling and reducing the scanning footprint. However, signal interferences from edges may still influence the testing results (Hoegh et al. 2019).

This study investigates how signal interferences from edges of cylindrical HMA specimens would influence dielectric measurements by using the time-of-flight method. The study aims to find proper sizes in preparing samples for laboratory testing. The study first presents a theoretical analysis to describe how the size of a cylindrical HMA specimen influences the accuracy of dielectric measurement using the time-of-flight method. The effect is further explored with numerical simulations and validated through experimental tests.

LABORATORY DIELECTRIC MEASUREMENT OF CYLINDRICAL HMA SPECIMENS

Figure 25 shows the testing setup for laboratory dielectric measurements of cylindrical HMA specimens. The GPR antenna is coupled with a Delrin acetal homopolymer block with a thickness of 1.52 inches (38.6 mm). The testing procedure involves four steps (Hoegh et al. 2019). Step 1 measures another acetal homopolymer block with a thickness of 1.52 inches (38.6 mm). Step 2 measures a steel plate instead of the second block. Step 3 measures a cylindrical HMA specimen without the second block or the steel plate. Step 4 measures the same HMA specimen with an additional steel plate on the top. Subtracting the measurement in step 2 from that in step 1 isolates the surface reflection. Subtracting the measurement in step 4 from the measurement in step 3 provides isolated bottom reflection from the HMA specimen. The time-of-flight is the timing difference of the first reference peak between the isolated surface and bottom reflections. Depending on how the subtraction was performed, the first reference peak can be either negative or positive.

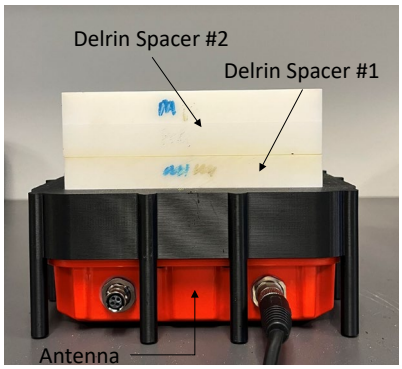

A. Step 1.

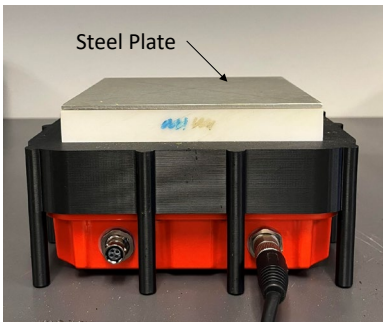

B. Step 2.

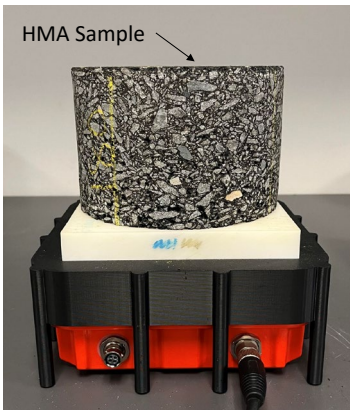

C. Step 3.

D. Step 4.

All images source: FHWA.

Figure 25. Photos. Testing setup for laboratory dielectric measurements of cylindrical HMA specimens.

Figure 26 shows a two-dimensional schematic step for the time-of-flight method, with origin O_1 being the surface reflection point, and O_2 the bottom reflection point. Without loss of generality, the ray paths of GPR signals are assumed to be straight lines. Accommodating the angles of refraction at interfaces by Snell's law will involve solving a set of fourth-order polynomial equations. The error introduced by the straight ray path assumption for typical asphalt dielectric and thickness was found in the order of 0.01 (Hoegh et al. 2019). The discrepancy is considered minimal, and Snell's law is ignored in calculations of the travel distance.

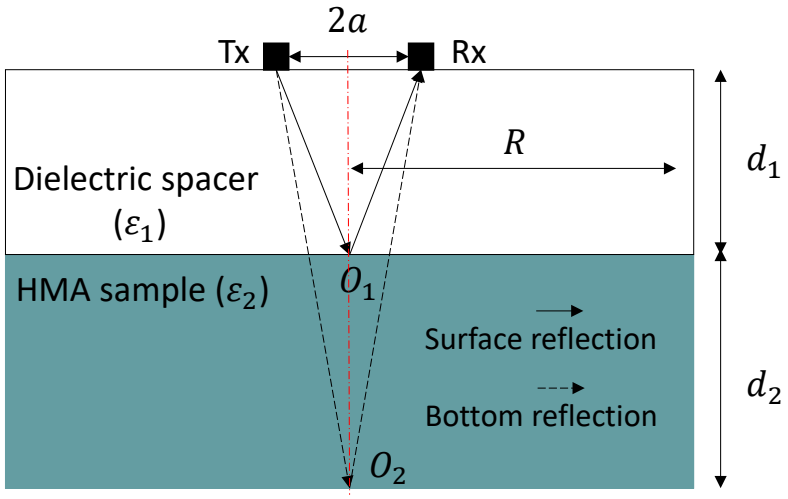

Source: FHWA.

Figure 26. Graph. Two-dimensional schematic step of dielectric measurements using the time-of-flight method.

In Figure 26, a is half of the separation distance between the *Tx* and the *Rx*; R is the radius of the HMA specimen; d_1 is the thickness of the dielectric spacer, and d_2 the thickness of the HMA specimen; and ε_1 denotes the dielectric of the spacer, and ε_2 the HMA specimen. By application of the straight ray path assumption, figure 27 and figure 28 give the two-way travel t of the surface reflection (t_1) and that of the bottom reflection (t_2), where $c \approx 0.3$ m/ns. After measurement of time-of-flight $\Delta t = t_2 - t_1$, figure 29 gives the dielectric of the HMA specimen,

$$t_1 = 2\sqrt{a^2 + d_1^2} \cdot \frac{\sqrt{\varepsilon_1}}{c}$$

Figure 27. Equation. Two-way travel *t* of the surface reflection.

$$t_2 = 2\sqrt{a^2 + (d_1 + d_2)^2} \cdot \frac{d_1\sqrt{\varepsilon_1} + d_2\sqrt{\varepsilon_2}}{(d_1 + d_2)c}$$

Figure 28. Equation. Two-way travel *t* of the bottom reflection.

$$\varepsilon_2 = \left[\frac{\Delta t \cdot c + 2\sqrt{a^2 + d_1^2} \cdot \sqrt{\varepsilon_1} - 2\sqrt{a^2 + (d_1 + d_2)^2} \cdot \frac{d_1}{d_1 + d_2} \cdot \sqrt{\varepsilon_1}}{2\sqrt{a^2 + (d_1 + d_2)^2} \cdot \frac{d_2}{d_1 + d_2}}\right]^2$$

Figure 29. Equation. Dielectric measurement using the time-of-flight method.

Multiple interferences from sample edges may exist. Figure 30 shows the ray paths for the internal reflection from the side surface (figure 30-A), the edge diffraction from the bottom edge (figure 30-B), and the critically refracted wave on the bottom surface (figure 30-C and figure 30-D). Figure 31 and figure 32 give the two-way travel t of the internal reflection from the side surface (t_3) and the edge diffraction from the bottom edge (t_4), respectively.

For the critically refracted wave on the right side of the bottom surface in figure 30-C (t_5), figure 33 gives the two-way travel t but requires $R - a - \frac{d_1 + d_2}{\sqrt{\varepsilon_2 - 1}} \geq 0$. The two way travel t of figure 30-D (t_6) uses figure 34 when $R + a - \frac{(d_1 + d_2)}{\sqrt{(\varepsilon_2 - 1)}} \geq 0$.

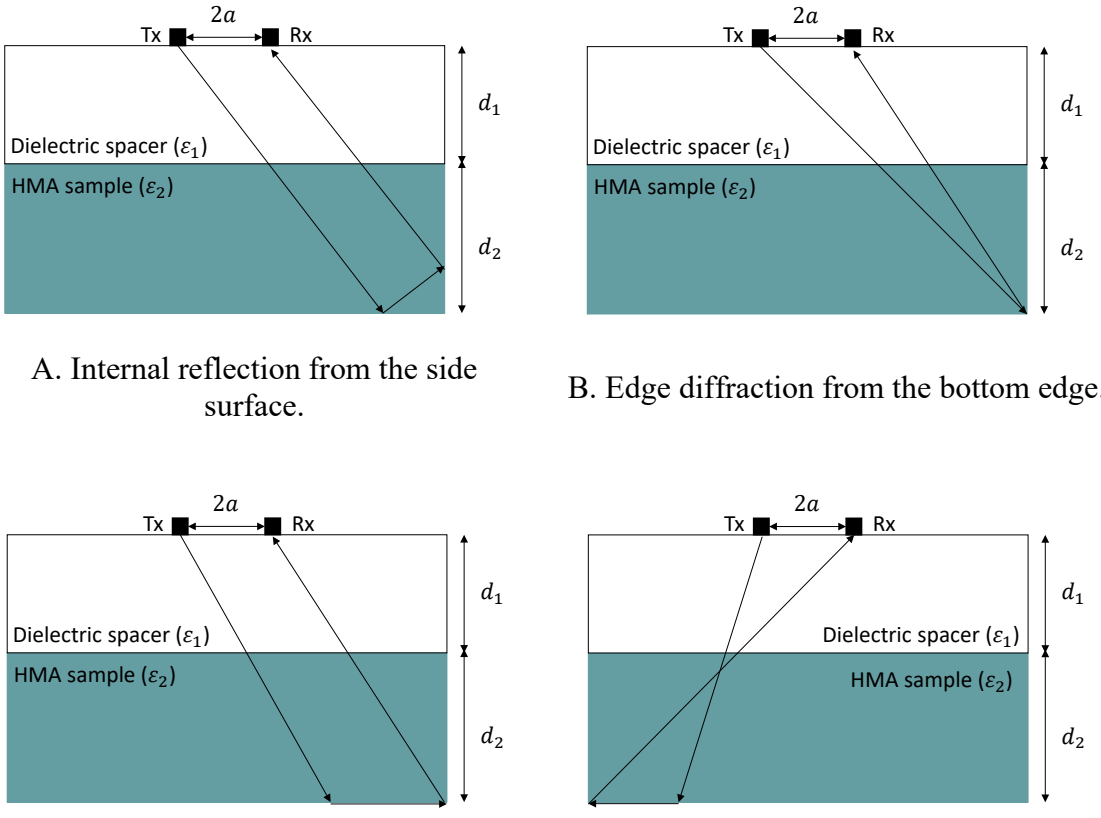

A. Internal reflection from the side surface.

B. Edge diffraction from the bottom edge.

C. Critically refracted wave on the right. side of the bottom surface.

D. Critically refracted wave on the left side of the bottom surface.

All images source: FHWA.

Figure 30. Graphs. Ray paths of interfering signals from sample edges.

$$t_3 = 2\sqrt{(d_1 + d_2)^2 + R^2} \cdot \frac{d_1\sqrt{\varepsilon_1} + d_2\sqrt{\varepsilon_2}}{(d_1 + d_2)c}$$

Figure 31. Equation. Two-way travel *t* for the internal reflection from the side surface.

$$t_4 = \left[\sqrt{(d_1 + d_2)^2 + (R - a)^2} + \sqrt{(d_1 + d_2)^2 + (R + a)^2}\right] \cdot \frac{d_1\sqrt{\varepsilon_1} + d_2\sqrt{\varepsilon_2}}{(d_1 + d_2)c}$$

Figure 32. Equation. Two-way travel *t* for the edge diffraction from the bottom edge.

$$t_5 = \left[\frac{(d_1 + d_2)\sqrt{\varepsilon_2}}{\sqrt{\varepsilon_2 - 1}} + \sqrt{(d_1 + d_2)^2 + (R + a)^2}\right] \cdot \frac{d_1\sqrt{\varepsilon_1} + d_2\sqrt{\varepsilon_2}}{(d_1 + d_2)c} + \left(R - a - \frac{d_1 + d_2}{\sqrt{\varepsilon_2 - 1}}\right) \cdot \frac{1}{c}$$

Figure 33. Equation. Two-way travel *t* for the critically refracted wave on the right side of the bottom surface.

$$t_6 = \left[\frac{(d_1 + d_2)\sqrt{\varepsilon_2}}{\sqrt{\varepsilon_2 - 1}} + \sqrt{(d_1 + d_2)^2 + (R - a)^2}\right] \cdot \frac{d_1\sqrt{\varepsilon_1} + d_2\sqrt{\varepsilon_2}}{(d_1 + d_2)c} + \left(R + a - \frac{d_1 + d_2}{\sqrt{\varepsilon_2 - 1}}\right) \cdot \frac{1}{c}$$

Figure 34. Equation. Two-way travel *t* for the critically refracted wave on the left side of the bottom surface.

Figure 35 compares the *t* of arrival of the first reference peak of the bottom reflection and onsets of internal reflection from the side surface, edge diffraction from the bottom edge, and critically refracted wave on the bottom surface for HMA specimens with sample heights (d_2) varying from 1.18 inches (30 mm) to 6.69 inches (170 mm). Figure 35 was generated by assuming R = 3 inches (76.2 mm), a = 0.87 inch (22 mm), d_1 = 1.52 inches (38.6 mm), ε_1 = 2.88, and ε_2 = 4.5. The arrival *t* of the first reference peak is about 0.34 ns later than the wave onset. The delay *t* of 0.34 ns and the value of the antenna separation distance of $2a$ = 1.73 inches (44 mm) were characterized experimentally by reference (Hoegh et al. 2019), representing the same model of antenna used in this study. Figure 35 shows that interferences from sample edges may arrive near or even slightly earlier than the arrival of the first negative peak of the bottom reflection. Such signal interferences may change both the magnitude and the timing of the reference peak. Any changes in the timing of the reference peak influence time-of-flight (Δt), which eventually influences the dielectric measurements in figure 29.

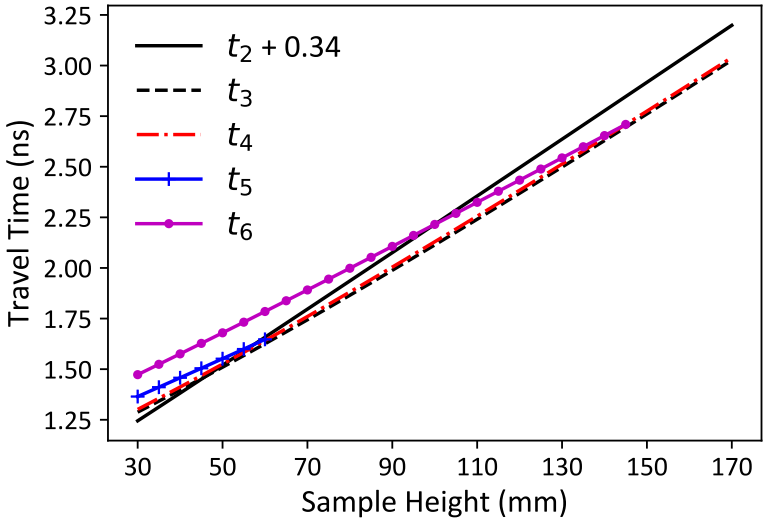

Source: FHWA.

Figure 35. Graph. Comparison of the *t* of arrival of interfering signals to that of the bottom reflection.

The analysis is not intended to conduct a complete survey but qualitatively demonstrates that interested signals (e.g., the bottom reflection) may accompany interferences from sample edges. The superposition of those signals may influence the accuracy of dielectric measurements using the time-of-flight method. Numerical simulations and experimental tests explored quantification of the edge effect on the error of dielectric measurements.

EDGE EFFECT IN DIELECTRIC MEASUREMENTS

Numerical Simulations

Numerical simulation was performed in gprMax (Warren, Giannopoulos, and Giannakis 2016), an open-source software that simulates EM wave propagation by solving Maxwell's equations via the finite-difference time-domain (FDTD) method. Studies have shown gprMax's capability to simulate the use of GPR for NDE of civil infrastructures, such as dielectric profiling of HMA and concrete bridge deck evaluations (Cao and Al-Qadi 2021; Pashoutani and Zhu, 2020). This study adopts gprMax for simulation of EM wave propagations in laboratory testing of cylindrical HMA specimens.

The simulation was based on a set of 2D FDTD models, considering the geometrical symmetry of HMA specimens. For simplicity, the HMA material was assumed to be homogeneous. The heterogeneity of the HMA material can result in wave scattering after the EM wave penetrates the sample surface (Cao and Al-Qadi 2021). The scattered wave may disturb the identification of signal interferences from sample edges. The material heterogeneity was considered in experimental tests described in the following subsections. schematically illustrates the simulation setup for FDTD models. The simulation compared two modeling scenarios: Figure 36-A modeled with actual sizes of HMA specimens and figure 36-B modeled with an infinite width, preventing the occurrence of signal interferences from sample edges. The differences in A-scans

(*t* series of EM waves) between the two scenarios isolate the interfering signals, quantifying potential measurement error caused by the edge effect.

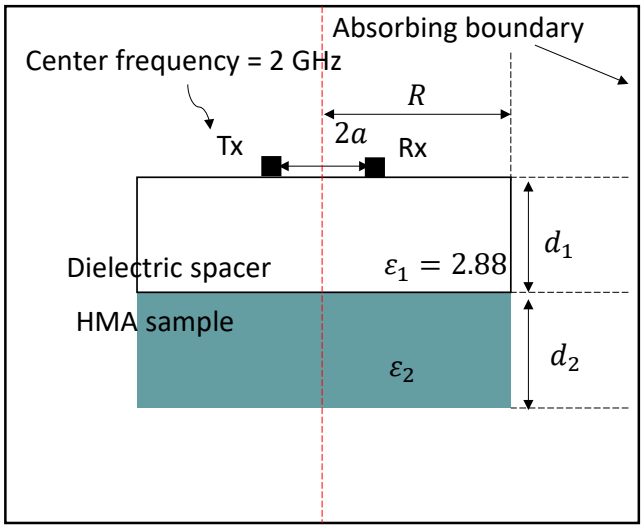

A. Considering the edge effect of HMA specimens.

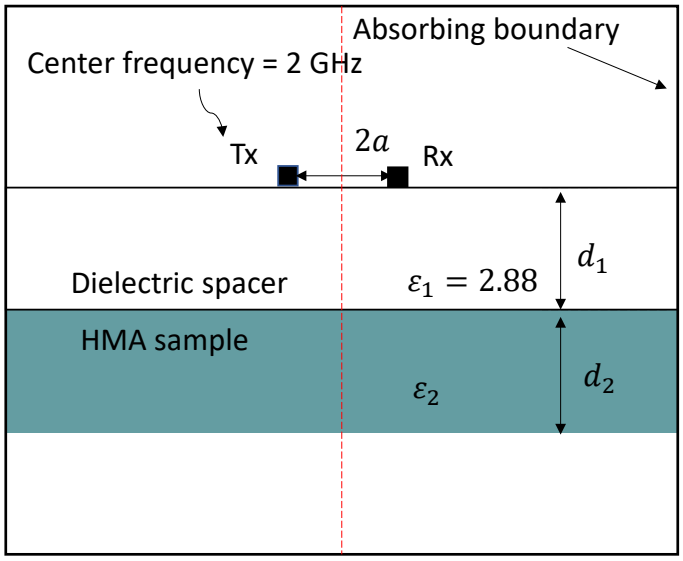

B. Ignoring the edge effect of HMA specimens.

All images source: FHWA.

Figure 36. Graphs. Simulation setups in gprMax.

The modeling of infinite width was achieved by extending the width of the HMA specimen to the boundary of the simulation domain, which satisfied the absorbing boundary conditions by using the perfectly matched layers in gprMax. The simulation domain in this study was created at 39.37 by 39.37 inches, or 1,000 by 1,000 mm, and the mesh size was 0.0393 inch, or 1 mm; the

domain size was found to be sufficiently large; and the mesh size was small enough to capture the EM wave propagation in HMA (about 60 times smaller than its wavelength at 2 GHz in materials of dielectric 6). The thickness and the dielectric for the dielectric spacer were 1.52 inches (38.6 mm) and 2.88, respectively; the antenna separation distance was 1.73 inches (44 mm), adopted from Hoegh et al. 2019. The antenna was simulated as a hertzian dipole, excited by a Ricker pulse voltage. The center frequency was set at 2 GHz according to the manufacturer's specification. The diameter of the HMA specimen was 6 inches (152.4 mm). The sample height varied from 1.18 to 6.69 inches or 30 to 170 mm for both scenarios. The dielectric of the HMA material was assumed to be 4.5, 5.5, and 6.5, covering a wide range of possible dielectric values of HMA reported in the literature (Cao and Al-Qadi 2021; Hoegh et al. 2018, 2019).

Figure 37 shows a typical calculation breakdown of the time-of-flight method using the numerical simulations of a 4.53-inch (115-mm)-high, 6-inch (152.4-mm)-diameter cylindrical HMA specimen. The four-step testing procedure isolates the reference peaks from the surface and the bottom reflection of the HMA specimen. The time-of-flight (Δt) for this example is 1.585 ns, which gives a dielectric of 4.51 based on figure 29, which is close to the assumed value of 4.5 in the simulation.

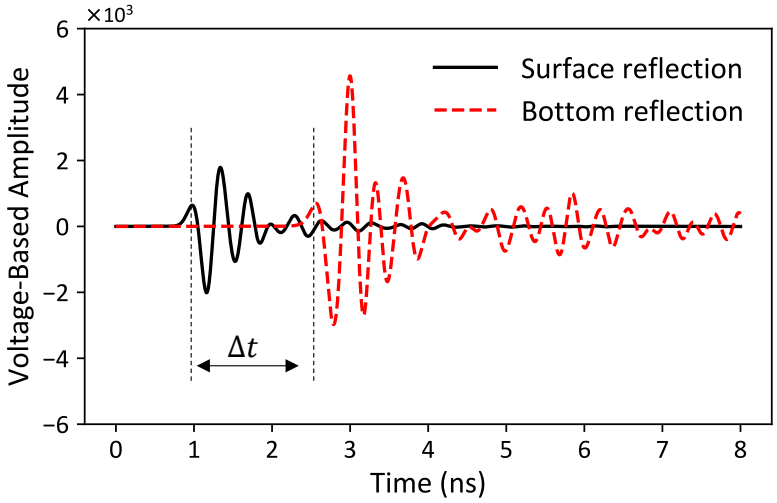

Source: FHWA.

Figure 37. Graph. Calculation breakdown in dielectric measurements based on numerical simulations of a 4.53-inch (115-mm)-high, 6-inch (152.4-mm)-diameter cylindrical HMA specimen.

Comparisons between the two simulated scenarios can reveal the interfering signals. The reference peak from the surface reflection of the HMA specimen was found to be uninfluenced by the interfering signals in numerical simulations. Figure 38 shows that the interfering signals typically arrive much later than the reference peak from the surface reflection. However, the edge effect affected mainly the reference peak from the bottom reflection of the HMA specimen.

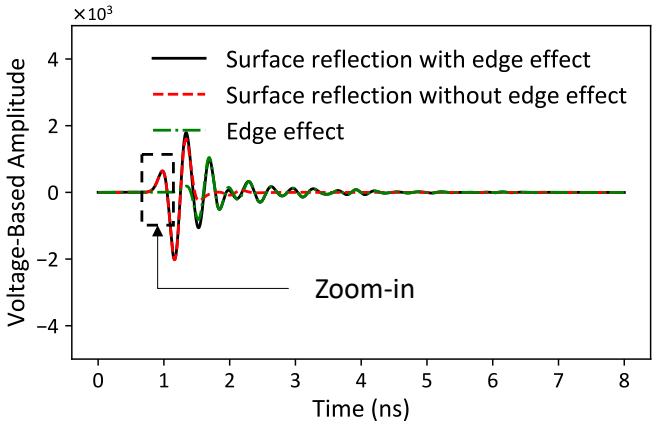

A. Full-time history from 0 to 8 ns.

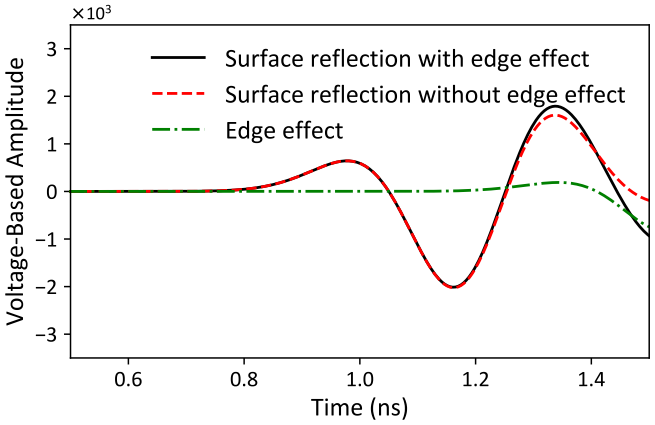

B. Zoom-in from 0.5 to 1.5 ns.

All images source: FHWA.
Note: The simulation was for a 3.15-inch (80-mm)-high, 6-inch (152.4-mm)-diameter cylindrical HMA specimen.

Figure 38. Graphs. Revealing edge effect on the surface reflection by subtracting simulated signals without from that with edge effect.

Figure 39 shows that the interfering signals superimposing the bottom reflection can shift the reference peak. In this example, the peak shift to the right results in a longer two-way travel t (Δt) and, thus, a larger dielectric. Such a shift in the reference peak leads to a change in the two-way travel t and is the main reason for the edge effect's influence on the dielectric measurement using the time-of-flight method.

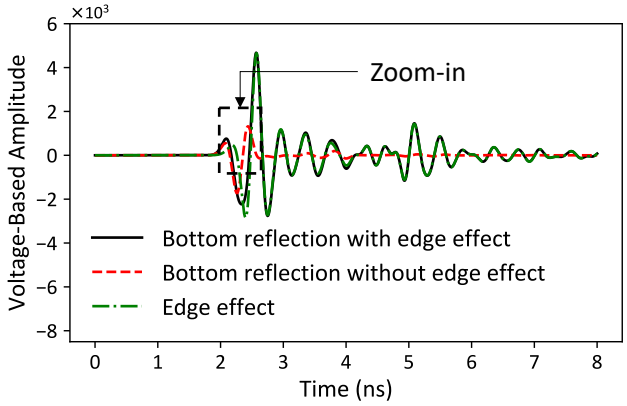

A. Full-time history from 0 to 8 ns.

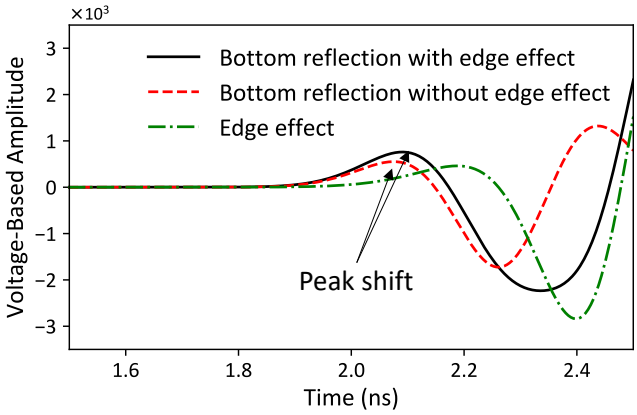

B. Zoom-in from 1.5 to 2.5 ns.

All images source: FHWA.
Note: The simulation was for an 3.15-inch (80-mm)-high, 6-inch (152.4-mm)-diameter cylindrical HMA specimen.

Figure 39. Graphs. Revealing edge effect on the bottom reflection by subtracting simulated signals without from that with edge effect.

Figure 40 summarizes the numerical results for cylindrical HMA specimens with 6-inch (152.4-mm) diameters but with varied heights from 1.18 inch (30 mm) to 6.69 inch (170 mm). The results are represented by the dielectric differences between the two simulated scenarios: measurements with and without the edge effect.

Figure 40 shows that, for samples with different dielectrics (4.5, 5.5, and 6.5), the edge effect results in slightly different variations in dielectric measurements. To evaluate the severity of the edge effect in dielectric measurements, this study adopted the AASHTO specification in which a limit of ±0.08 is set as the operational requirement for general purposes of using GPR (PP 98 (AASHTO 2019)). In terms of the AASHTO limit, the edge effect is severest for shorter HMA specimens with a height of less than 3.93 inches (100 mm). The numerical simulation suggests that increasing the HMA sample height—preferably to greater than 4.53 inches (115 mm)—can mitigate the edge effect. The finding was verified through experimental tests.

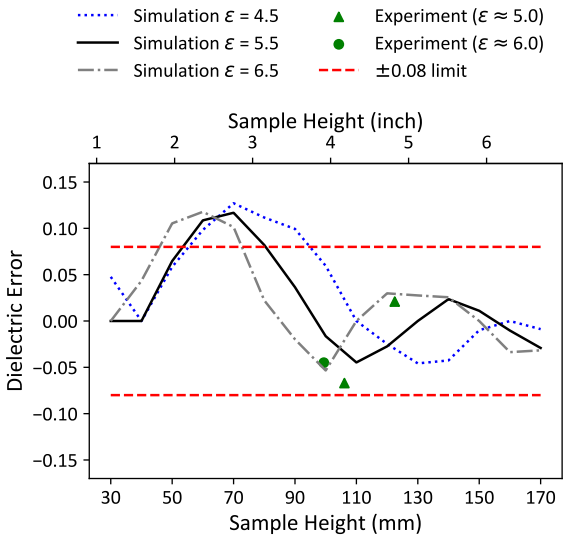

Source: FHWA.

Figure 40. Graph. Dielectric differences resulted from the edge effect of cylindrical HMA specimens in 6-inch (152.4-mm) diameter but with varied heights from 1.18 inches (30 mm) to 6.69 inches (170 mm).

Experimental Tests

The challenge in the experimental testing is to isolate the edge effect while maintaining the same of other factors that may also influence the dielectric measurements, such as aggregate sources and density (Sias and Dave 2023; Teshale et al. 2020). This study resolved the challenge by first testing an HMA slab and then testing a core sample that was drilled out from the center of the slab. The drilling process ensures the two testing samples share the same material mix and density in the testing region. The differences in comparing the two dielectric measurements reveal the edge effect. As a side-by-side comparison to the numerical simulations, the HMA slab represents the scenario with infinite width, and the core sample represents the scenario with actual specimen sizes.

The fabrication of infinitely wide HMA slabs is practically infeasible. Alternatively, the HMA slab was designed to have sufficient length and width but varied heights. Such a design generates a sufficient delay so that the interfering signals from the slab edges arrive later than the reference peaks. The sufficient delay ensures the calculation of time-of-flight (Δt) is not affected, and so does the dielectric measurement. In this study, the HMA slabs are 10.23 inches (260 mm) wide and 12.60 inches (320 mm) long. The widths and lengths of HMA slabs were numerically confirmed to be sufficient. Three slabs were fabricated at heights of 3.91, 4.18, and 4.82 inches, or 99.36, 106.10, and 122.49 mm. Figure 41 shows the fabricated HMA slabs with the cores drilled from the center of the corresponding slab.

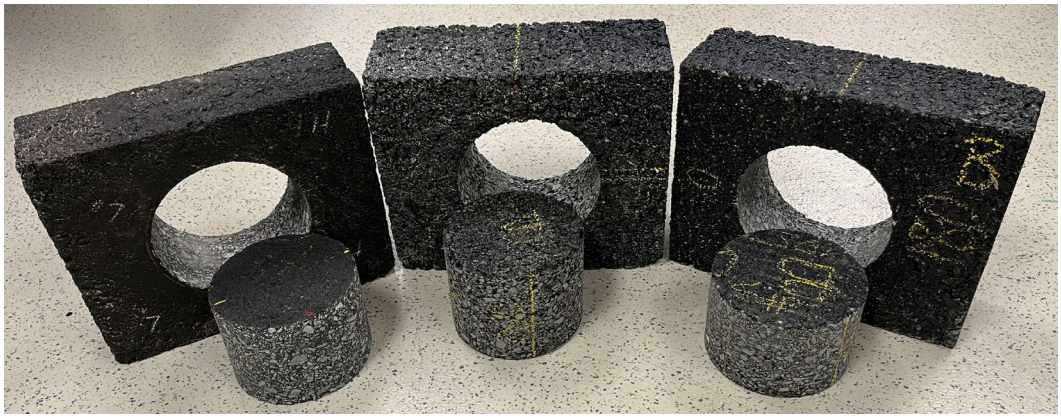

Source: FHWA.

Figure 41. Photo. Fabricated HMA slabs with cores drilled from center of corresponding slab.

The experimental testing results are scattered in figure 40. The ε's for the HMA slabs at 3.91, 4.18, and 4.82 inches—or 99.36, 106.10, and 122.49 mm, respectively—were 5.91, 5.03, and 5.01, respectively, while the ε's for the corresponding cores were 5.86, 4.96, and 5.03, respectively. As a result, the dielectric differences by subtracting the ε's of slab samples from those of the corresponding core samples were −0.04, −0.07, and 0.02. The experimental results validated the numerical simulations that, for HMA samples with 6-inch (152.4-mm) diameters, a sample shall be higher than 3.93 inches (100 mm) to reduce the measurement error and therefore be within the AASHTO limit. A height of 4.53 inches (115 mm) or higher is preferable to control a measurement error within ±0.05.

DISCUSSIONS

Smaller Diameters of Cylindrical Specimens

Because of practical limitations, field cores may also come with smaller diameters, such as 4 inches (101.6 mm). Although smaller diameters for field cores may save time and effort in coring, the edge effect can be much severer than the 6-inch (152.4-mm) cores. That aspect was investigated numerically by changing the HMA sample diameter to 4 inches (101.6 mm). Figure 42 summarizes numerical results for cylindrical HMA specimens with 6-inch (152.4-mm) diameters but with varied heights from 1.18 inches (30 mm) to 6.69 inches (170 mm). The dielectric differences due to the edge effect at nearly all heights exceed the AASHTO limit (more than ±0.2) regardless of the HMA sample dielectric's being 4.5, 5.5, or 6.5. Unlike HMA samples

with diameters of 6 inches (152.4 mm), samples with 4-inch (101.6-mm) diameters do not benefit from increasing sample height to control the edge effect to be within ±0.08. That finding suggests the diameter of cylindrical HMA specimens shall be maintained at 6 inches, or 152.4 mm.

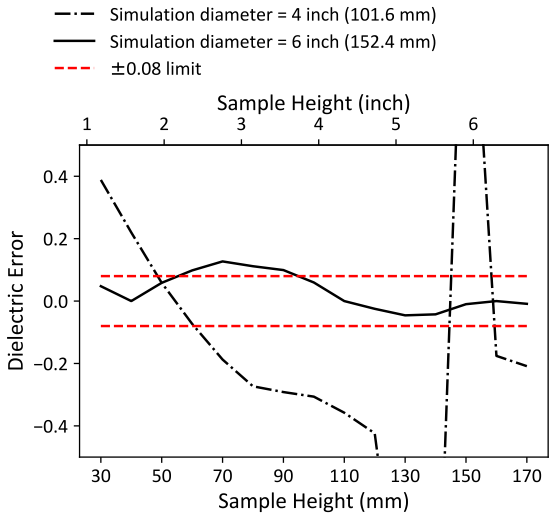

A. Sample $\varepsilon = 4.5$.

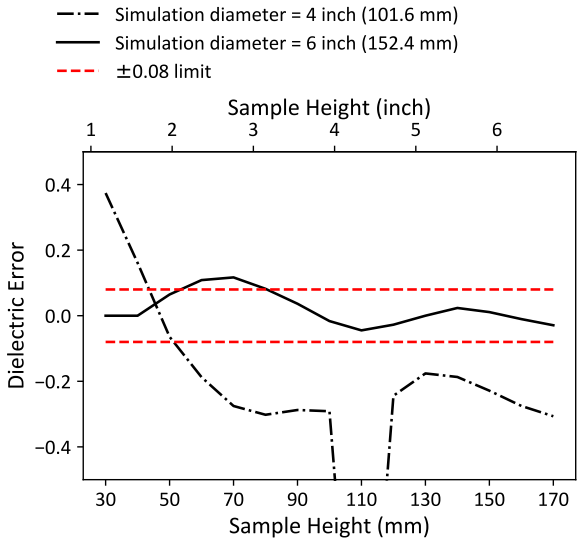

B. Sample $\varepsilon = 5.5$.

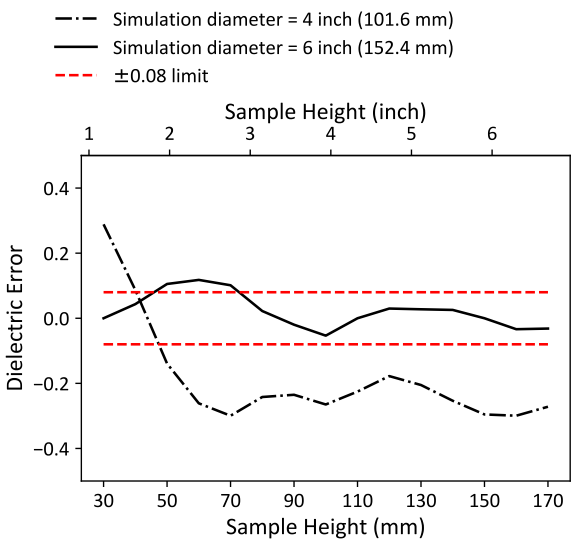

C. Sample $\varepsilon = 6.5$.

All images source: FHWA.

Figure 42. Graphs. Dielectric differences resulted from the edge effect of cylindrical HMA specimens in 4-inch (101.6-mm) and 6-inch (152.4-mm) diameters but with varied heights from 1.18 inches (30 mm) to 6.69 inches (170 mm).

Antenna Perspective to Mitigate Edge Effect

The center frequency of the GPR antenna was 2 GHz for both numerical simulations and experimental tests. Additional sets of numerical simulations were conducted to investigate the influence of antenna frequency on edge effect. The simulation explored three center frequencies at 1.5, 2, and 2.5 GHz. Figure 43 summarizes the numerical results, which indicate the dielectric differences caused by the edge effect become lower at 2.5 GHz center frequency, while becoming larger at 1.5 GHz compared with the baseline of 2 GHz. That observation can be explained intuitively because a higher center frequency normally results in a narrower pulsed waveform, thereby exposing a narrower t window for the reference peak to be influenced by other signals. Interestingly, the 2.5-GHz antenna controls the edge effect so that it is within the ±0.08 limit at all heights. Increasing the antenna frequency may alleviate the height restrictions of 6-inch (152.4-mm) samples. However, informal discussions with GPR manufacturers reveal difficulties in changing the antenna frequencies of current GPR designs. Future GPR development might benefit from using a higher center frequency to mitigate the edge effect.

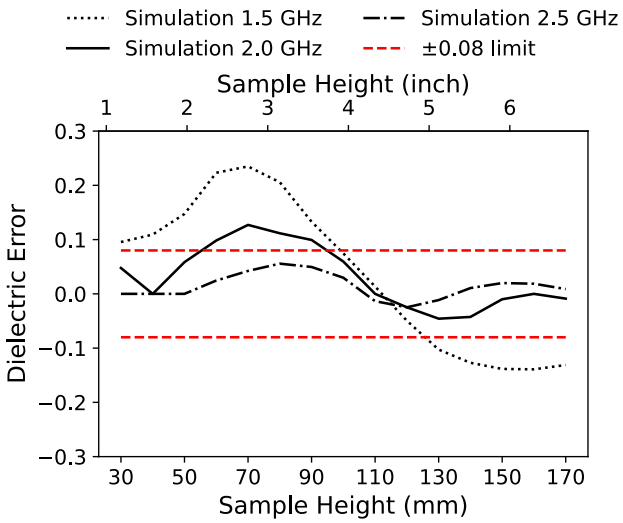

A. Sample $\varepsilon = 4.5$.

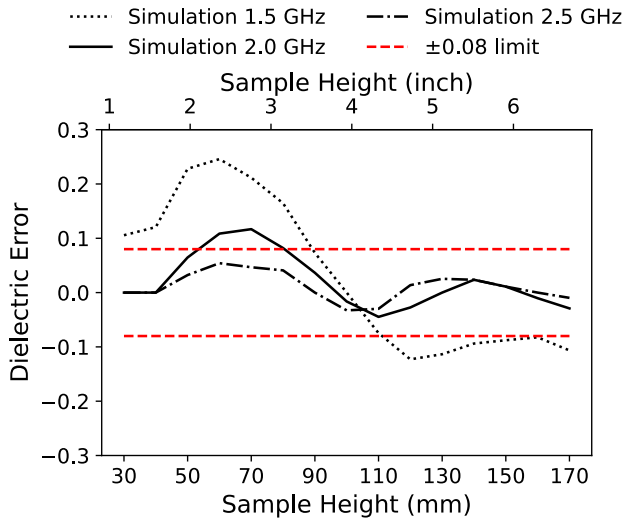

B. Sample $\varepsilon = 5.5$.

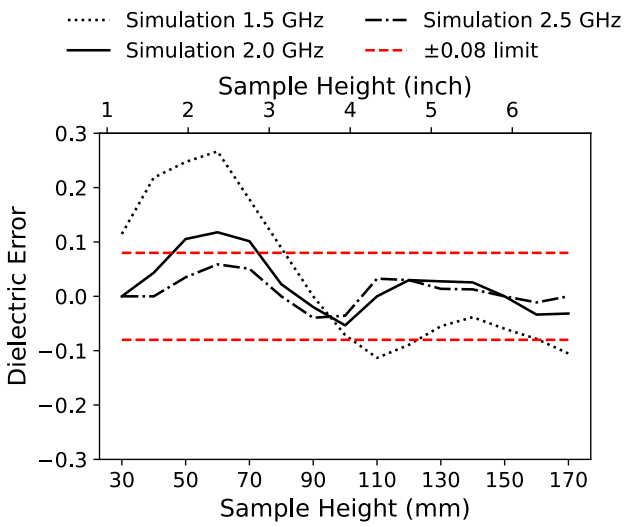

C. Sample $\varepsilon = 6.5$.

All images source: FHWA.

Figure 43. Graphs. Dielectric differences resulted from the edge effect of cylindrical HMA specimens in 6-inch (152.4-mm) diameter but with varied heights from 1.18 to 6.69 inches, or 30 to 170 mm.

Limitations and Future Work

In numerical simulations, the GPR antenna was modeled as a hertzian dipole, representing a theoretically infinitesimally small dipole antenna. Although the GPR for the presented experimental tests was a small, dipole-type antenna, some discrepancies still exist between the numerical simulations and experimental tests. In addition, the HMA material was assumed to be homogeneous. Future work may need to explore advanced numerical modeling for more representative models of the antenna and HMA material—such as considering the heterogeneous nature of aggregates—to close the discrepancies.

REMARKS

Density profiling using GPR for asphalt pavement has been a rising trend that is benefiting the transportation sector with safer, more efficient, and wider coverages in compaction assessments of roadways. This study contributes to a fundamental understanding of technologies that use dielectric measurements—especially for cylindrical HMA specimens. The limited size of cylindrical HMA specimens (filed cores or compacted samples) can result in edge effect in measurements. This study evaluates the edge effect through numerical simulations and experimental tests. The main findings are as follows:

- The edge effect represents interfering signals from sample edges accompanying the data collection. The edge effect can shift the reference peak that is used for measuring the two-way travel t of GPR signals, leading to a change in dielectric measurement using the time-of-flight method.

- For cylindrical HMA samples with 6-inch (152.4-mm) diameters, a sample height of 4.53 inches (115 mm) or higher is preferable to reduce the edge effect by controlling the measurement error to be within ±0.05 dielectric.

- Decreasing the diameter of cylindrical HMA samples from 6 inches (152.4 mm) to 4 inches (101.6 mm) can result in a much larger measurement error. The study results suggest maintaining the diameter at 6 inches (152.4 mm) for dielectric measurement.

CHAPTER 5. STUDY ON EMPIRICAL MODELS FOR CORRELATING DIELECTRIC TO ASPHALT COMPACTION

Part of this chapter has been submitted as a conference paper to the 11th International Conference on the Bearing Capacity of Roads, Railways and Airfields (Rashidi and Azari 2022).

INTRODUCTION

ε_{HMA} can be related to the ε of its constituents by using dielectric mixing models (Al-Qadi et al. 2010). Based on assumptions related to model development, the literature presents numerous dielectric mixing models (Al-Qadi et al. 2010; Araujo et al. 2016; Fernandes et al. 2017; Leng, Al-Qadi, and Lahouar 2011). For estimating the density of HMA, Al-Qadi developed a modified Rayleigh, Böttcher, and complex-refractive-index model that requires information about the dielectric properties of HMA constituents (Al-Qadi et al. 2010).

The Rayleigh mixing model and several other models the literature has developed rely on the formal arrangement of inclusions (i.e., air void), and they are inadequate when applied to the random arrangement of bodies (Pearce 1955). The Böttcher equation is valid only for a limited range of ε (Pearce 1955). Due to such limitations, Leng et al. (2011) recommend back-calculating the dielectric properties of aggregates from at least one core sample to reduce prediction errors.

Aside from dielectric mixing models, purely empirical models relate AC to the ε_{HMA}. The simplest models are linear (figure 44) or exponential decay functions (figure 45), where AC is the air-void content in HMA, and a, b, c, and d are fitting parameters.

$$AC = a \times \varepsilon_{HMA} + b$$

Figure 44. Equation. Linear correlation between air-void contents and ε_{HMA} pavements.

$$AC = c \times e^{-d \times \varepsilon_{HMA}}$$

Figure 45. Equation. Exponential decay correlation between air-void contents and ε_{HMA} pavements.

Depending on the range of core data, figure 44 may fit data quite well. On the other hand, according to extensive studies by Finnish researchers Saarenketo and Scullion (2000), figure 45 provides a reasonable relationship between the AC and ε_{HMA}. Figure 44 and figure 45 typically do not reach 100-percent AC at the ε of 1. The two equations can be considered estimations of relationships between AC and ε_{HMA} in certain ranges, which can be especially problematic when a prediction of AC outside the fitting range is desired.

To mitigate issues associated with figure 45, an enhanced model (figure 46, where *E*, *F*, and *G* are fitting parameters) includes an additional fitting parameter to force AC = 100 percent at the dielectric of 1. Such an approach increases the model's complexity, and it does not necessarily result in a better fit than figure 45 at low AC (i.e., AC of less than 10 percent) (Hoegh et al. 2018).

$$AC = e^{\left(-E\left(F\left|\frac{1}{\varepsilon_{HMA}-G}-\frac{1}{1-G}\right|-1\right)\right)}$$

Figure 46. Equation. An enhanced model to correlate ε to air-void contents of HMA pavements.

Recently, a five-parameter logistic regression equation (MnDOT) was adapted (figure 47, where *M*, *N*, and *K* are fitting parameters with no physical meaning) to relate AC to the ε_{HMA} (Steiner et al. 2020). Compared with figure 46, the model tends to fit the experimental data better (Steiner et al. 2020), but, similar to figure 46, the model suffers from increased complexity (compared with figure 44 and figure 45).

$$AC = \frac{0.2}{\left(1+\left(\frac{\varepsilon_{HMA}}{M}\right)^{N}\right)^{K}} + \frac{0.0008}{\varepsilon_{HMA}-1}$$

Figure 47. Equation. MnDOT model to correlate ε to air-void contents of HMA pavements.

This chapter suggests, first, application of the Pearce empirical dielectric mixing model for estimation of HMA AC (Pearce 1955). The chapter then assesses the performance of empirical relationships in fitting to field datasets. Engineers and practitioners may deem such an assessment useful in their selection of a correlation model for their field applications. Furthermore, the chapter investigates models' capability to predict the AC of HMA at high and low dielectric values.

HMA AS A TWO-PHASE MATERIAL

Although HMA is made of aggregate, binder, and air, in this study HMA is considered a two-phase material to be used in the Pearce empirical dielectric mixing model (Pearce 1955). Here the host phase is aggregated with their surrounding asphalt binder, and air voids are considered the second phase. Then the decrease in ε_{HMA} with an increase in its AC can be expressed according to figure 48, in which ε_{ff} is the effective ε (i.e., the εHMA); ε_h is the ε of the host (i.e., the ε of aggregates with their surrounding binder); ε_{in} is the ε of inclusion (i.e., air); *V* is the volume fraction of inclusion; and *k* is an empirical factor not necessarily related to the shapes of inclusions (Pearce 1955).

$$\frac{\varepsilon_{ff}-\varepsilon_h}{\varepsilon_{in}-\varepsilon_h} = \frac{(1-k)V}{(1-kV)}$$

Figure 48. Equation. Pearce model to correlate ε to air-void contents of HMA pavements.

The Pearce model fulfills the conditions at $V = 0$, where $\varepsilon_{ff} = \varepsilon_h$, and at $V = 100$ percent, where $\varepsilon_{ff} = \varepsilon_{in}$. When fitting to the experimental data, the model's complexity is identical to equations 2 and 3, since it has only two unknown parameters: ε_h and k. As such, in theory, only two cores are required for fitting purposes. A larger number of cores would reduce uncertainty in the fitting process.

For HMA, it is desired to rearrange the Pearce model, in which the left-hand side of the equation is AC, and the right-hand side is a function of ε_{HMA}. Setting $\varepsilon_{ff} = \varepsilon_{HMA}$, $\varepsilon_{in} = 1$, and V = AC achieves figure 49.

$$AC = \frac{\varepsilon_h - \varepsilon_{HMA}}{(\varepsilon_h - 1) - k(\varepsilon_{HMA} - 1)}$$

Figure 49. Equation. Air-void contents using the Pearce model.

Figure 50 shows the relationship between AC and ε_{HMA} for different k values. ε_{HMA} is varied from 1 (ε of air) to $\varepsilon_h = 1$. In practice, depending on the dielectric properties of aggregates and binder, ε_h is likely in the range of 4–7. Except for $k = 0$, the Pearce model generates a nonlinear relationship between AC and ε_{HMA}. For low AC and a limited dielectric range, the Pearce model may be estimated using a linear relationship between AC and ε_{HMA}.

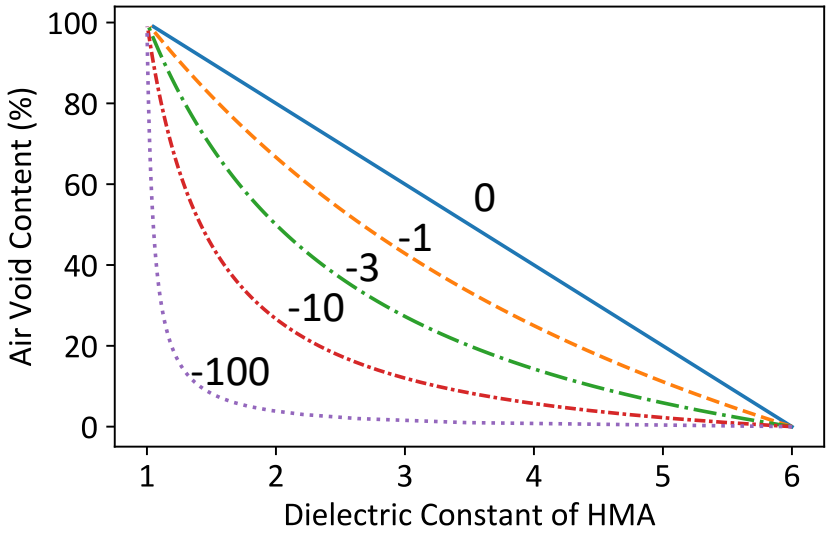

Source: FHWA.

Figure 50. Graph. Relationship between AC and (ε_{HMA}) estimated using the Pearce dielectric mixing model.

COMPARING THE FITTING PERFORMANCE OF EMPIRICAL RELATIONSHIPS

To compare the performance of empirical models in estimating the AC of HMA, linear (figure 44), exponential (figure 45), HD (figure 46), MnDOT (figure 47), and Pearce (figure 48) models are fit to the 23 field datasets. The first dataset was selected from the work of Finnish researchers Saarenketo and Scullion (2000), which has shown an exponential relationship between the ε and AC of a large number of cores. Four datasets were selected from the Strategic Highway Research Program (SHRP2) report (Sebesta, Saarenketo, and Scullion 2012). The Texas A&M Transportation Institute provided 12 datasets. Six of the datasets were also reported in Wilson, Sebesta, and Scullion (2019). Four datasets were obtained from Khazanovich et al. (2017). The two last datasets were provided by the Ohio Department of Transportation (ODOT). Each dataset has information on the AC and ε of at least eight cores. Briefly, the SHRP2 data were collected on three regions of AASHTO. Except for region 1, where the ε was measured using 1-GHz and 2.2-GHz antennas, the ε of asphalt in regions 2 and 3 was estimated using a 1-GHz antenna (Sebesta, Saarenketo, and Scullion 2012). The data collected by the Texas A&M Transportation Institute, those reported by Khazanovich et al. (2017), and the ones from ODOT were collected using an RDM manufactured by GSSI (Wilson et al. 2019). RDM collects data with 2-GHz antennae.

Models were fit to the data by means of the least-squares approach, and their corrected Akaike information criterion (AIC) was estimated according to figure 51, in which SSE is the sum of squared errors, n is the number of samples (i.e., cores), p is the number of model parameters plus one (for linear, exponential, and Pearce models, $p = 3$; for the enhanced and MnDOT models, $p = 4$). Lower AIC is preferred.

$$Corrected\ AIC = n\left\{ln\left(\frac{SSE}{n}\right) + ln(2\pi) + 1\right\} + \frac{2np}{(n-p-1)}$$

Figure 51. Equation. Definition of corrected AIC.

The corrected AIC balances goodness of fit and model complexity as it rewards minimizing the SSE while penalizing for the increased number of model parameters. Thus, AIC provides a basis for comparing models that vary in number of parameters. Best models were selected based on their $\Delta AIC = AIC - \min AIC \leq 2$, which indicates substantial support (evidence) for the best approximating models among candidates (Burnham and Anderson 2001).

The total corrected AIC for the linear, exponential, enhanced, MnDOT, and Pearce models were −2063.50, −2034.20, −1893.80, −1924.30, and −2063.10, respectively. The large values of the corrected AIC for the MnDOT model make the model less favorable for fitting to the data. Similarly, the large AIC values of the enhanced model reflect the model's excessive complexity (and lack substantial SSE reduction) for fitting the data into the range of core values.

COMPARING THE PREDICTIVE PERFORMANCE OF EMPIRICAL RELATIONSHIPS

To investigate the predictive performance of empirical models at low and high dielectric values, the core data were sorted in descending order according to their ε. Then approximately 70 percent of the data was used for training, and approximately 30 percent for testing the behavior of models. Such training-test partitioning is common in the literature (Akay 2009). Then models were fit to the training portion of the data, and the mean squared prediction error (MSPE) was estimated according to figure 52, in which n is the number of testing points; AC_i is AC at the ith testing point; and AC_l is AC at the ith testing point predicted by a model.

$$MSPE = \sum_{i=1}^{n} \frac{\left(AC_i - \widehat{AC_i}\right)^2}{n}$$

Figure 52. Equation. Definition of mean squared prediction error.

The predictive performances of models were evaluated separately for both relatively high and low dielectric samples. High dielectric samples were those with the top 30 percentile of ε, and low dielectric samples are the bottom 30 percentile of ε.

The MPSE for high dielectric samples of the linear, exponential, enhanced, MnDOT, and Pearce models were 1.46, 1.40, 1.27, 1.20, and 1.29×10^{-4}. Given the distribution of errors, the performance of models seems comparable for high dielectric values. That comparability is consistent with the typical convergence of models at high ε.

However, for low dielectric values wherein models tend to deviate from one another. The MPSE for low dielectric samples of the linear, exponential, enhanced, MnDOT, and Pearce models were 2.60, 10.2, 4.67, 7.45, and 2.80×10^{-4}. Given the distribution of errors, the exponential model may predict the AC of HMA substantially higher than the rest of the models. Overall, for low dielectric values, linear and Pearce models may result in the lowest prediction errors, followed by HD and MnDOT models and then the exponential model.

The results show Pearce and linear models behave similarly. However, at lower dielectric values, parameter k in the Pearce model allows for the nonlinear behavior of the model to reach 100-percent air void at the ε of 1. On the other hand, extrapolation of the linear model to low dielectric values (high AC) ignores the increased interaction between air voids and typically results in an estimation of inaccurate AC.

REMARKS

The study evaluated the performance of various empirical models that correlate the ε to the air-void contents in HMA. The results suggest that the linear regression model maintains a lower RMSE than other investigated nonlinear exponential models. A linear regression model is simple to use, and it can reasonably predict the AC of HMA at typical ranges of ε.

CHAPTER 6. FIELD IMPLEMENTATION: GREENBELT PARK PAVING PROJECT

INTRODUCTION

A field implementation of the DPS was applied to a paving project in Greenbelt, MD. Field testing followed MnDOT's data collection protocols (MnDOT 2024b), including pre- and postpaving procedures, field dielectric quality assurance procedures, and field routine collection protocols. Since the paving contractor did not take more than one core for quality assurance purposes, the development of a correlation curve to relate core dielectric values to AC was not feasible. Therefore, the research team followed the protocol for relating dielectric values to the AC of SGC samples. To fabricate SGC samples, the research team collected the plant-produced mixture from the back of the paver on each day of paving. The research team passed the material to the FHWA Asphalt Binder and Mixtures Laboratory (ABML) at Turner-Fairbank Highway Research Center for SGC sample fabrication. Through measurement of the ε of SGC samples and the AC of SGC samples, the research team developed the dielectric-to-air-void correlation curve. The AC of SGC samples were measured following D6752 (ASTM 2009) and T331 (AASHTO 2002). The use of SGC specimens mitigated the demand for destructive measures.

RESULTS

The data were collected on May 11, 2021. To make sure that all sensors provide consistent measurement that complies with PP98 (AASHTO 2019), the swerve test was performed. Table 2 and table 3 show swerve tests' statistical data for two consecutive trials in the field. Since the daily paving was limited to the Holly picnic parking area, which was approximately 48 ft wide by approximately 400 ft long, the research team were often a lane away from the final compacter roller during the scanning (figure 53). However, the research team noticed notable moisture and vibrations from the compactor. Dielectric measurement results are shown as a condition map (figure 54). The research team used the plant-produced mixture to fabricate nine SGC samples in three main ranges of dielectrics: 6.12, 5.7, and 5.3. The correlation curve was developed using a linear model (figure 55). By application of the correlation to dielectric measurements, the AC for the field data was obtained (figure 56).

Table 2. First swerve tests' statistical results.

Lateral Offset	Start Distance (ft)	End Distance (ft)	Start Station	End Station	Average Dielectric	Median Dielectric	Min. Dielectric	Max. Dielectric
2L	33	100	00+33	01+00	5.37	5.34	4.88	6
2L	100	200	01+00	02+00	5.57	5.58	4.94	6.42
2L	200	300	02+00	03+00	5.59	5.57	5.06	6.21
4L	33	100	00+33	01+00	5.43	5.45	4.86	5.87
4L	100	200	01+00	02+00	5.54	5.53	4.94	6.75
4L	200	300	02+00	03+00	5.64	5.65	4.94	6.13
6L	33	100	00+33	01+00	5.45	5.45	4.95	6.01
6L	100	200	01+00	02+00	5.59	5.59	5.11	7.27
6L	200	300	02+00	03+00	5.73	5.73	5.3	6.14

Max. = maximum; Min. = minimum.

Table 3. Second swerve tests' statistical results.

Lateral Offset	Start Distance (ft)	End Distance (ft)	Start Station	End Station	Average Dielectric	Median Dielectric	Min. Dielectric	Max. Dielectric
2L	33	100	00+33	01+00	5.37	5.34	4.88	6
2L	100	200	01+00	02+00	5.57	5.58	4.94	6.42
2L	200	300	02+00	03+00	5.59	5.57	5.06	6.21
4L	33	100	00+33	01+00	5.43	5.45	4.86	5.87
4L	100	200	01+00	02+00	5.54	5.53	4.94	6.75
4L	200	300	02+00	03+00	5.64	5.65	4.94	6.13
6L	33	100	00+33	01+00	5.45	5.45	4.95	6.01
6L	100	200	01+00	02+00	5.59	5.59	5.11	7.27
6L	200	300	02+00	03+00	5.73	5.73	5.3	6.14

Source: FHWA.

Figure 53. Photo. An NDE laboratory research engineer performing DPS scanning.

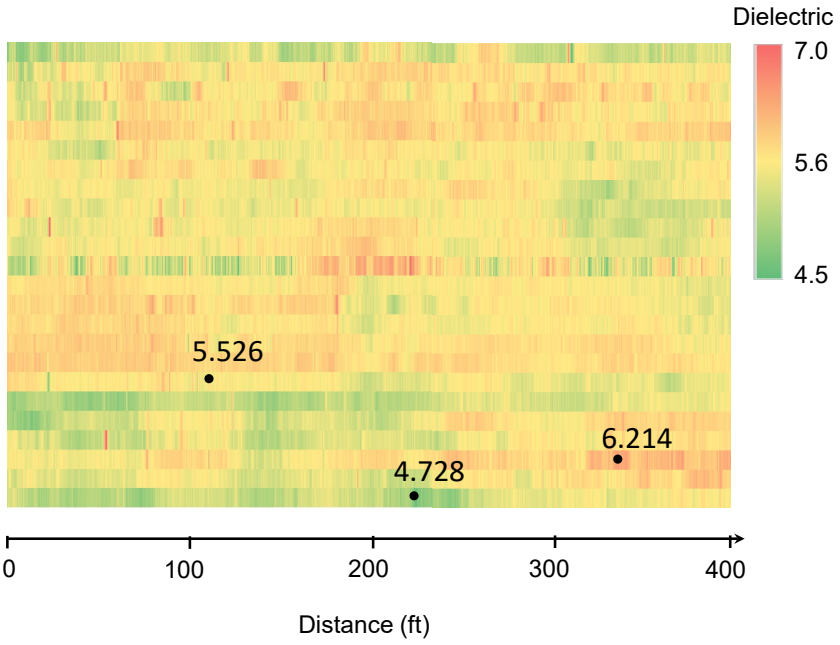

Source: FHWA.

Figure 54. Graph. Measured ε for the scanned paving area.

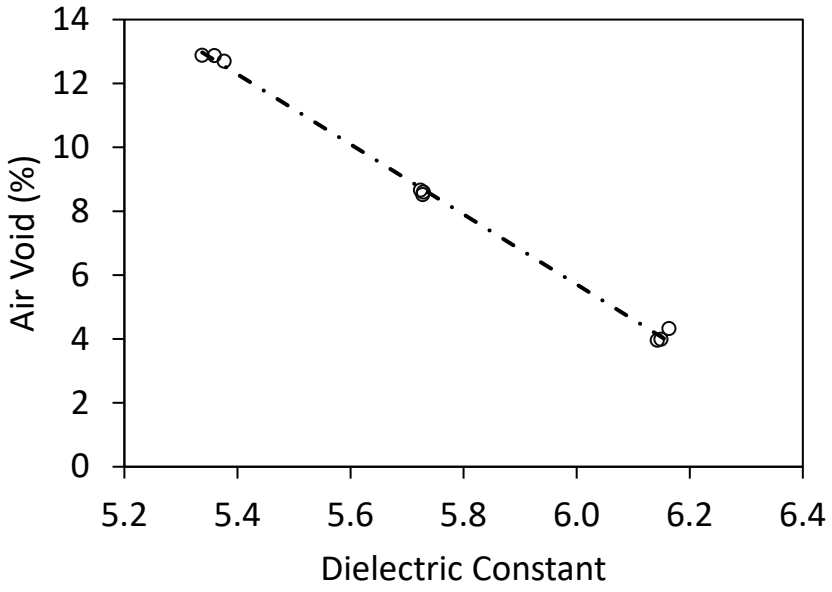

Source: FHWA.
Note: Trend equation: $y = -10.968x + 71.51$, $R^2 = 0.9974$.

Figure 55. Graph. Linear correlation model from nine SGC samples.

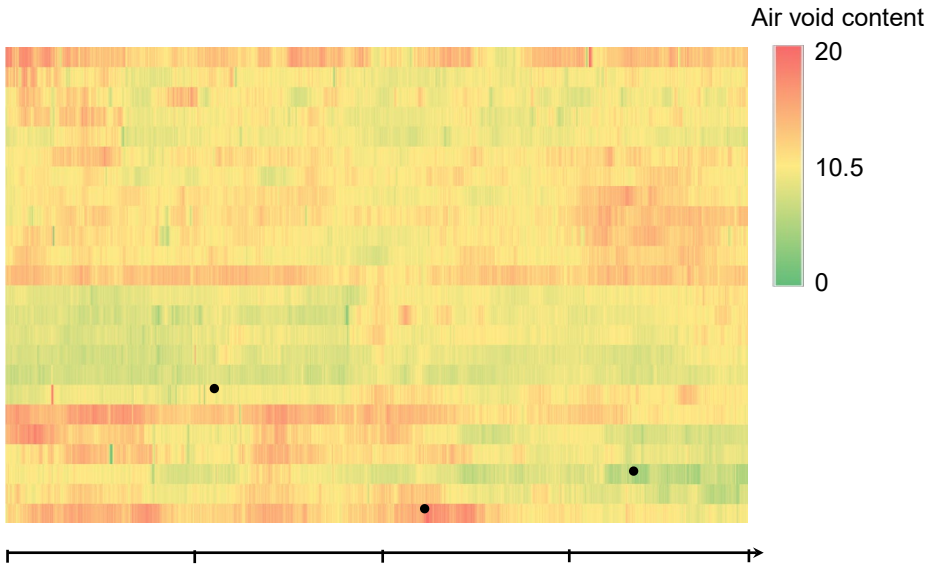

Source: FHWA.

Figure 56. Graph. Measured ACs for the scanned paving area.

REMARKS

This study reported on the field application of DPS on the Greenbelt Park paving project in Maryland. The takeaways from the field testing were as follows:

- Performing field dielectric equipment checks is crucial for obtaining quality data during field testing. The procedure should be performed several times during each day of paving.
- Linear field dielectric collection type (line test) for quality checks of sensors was found more versatile because testing all three sensors along the same path could better reveal differences between sensor measurements.
- Asphalt's sticking to DPS wheels results in inaccurate distance measurements, and asphalt must be removed or prevented from sticking during tests.
- Debris, leaves, or other objects must be removed from the pavement surface before tests.
- Tests should be performed away from the final roller to prevent any possibly remaining moisture and excessive vibrations.

REFERENCES

AASHTO. 2002. *Standard Method of Test for Bulk Specific Gravity of Compacted Bituminous Mixtures Using Saturated Surface-Dry Specimens T 166*. Washington, DC: American Association of State Highway and Transportation Officials.

AASHTO. 2019. *Asphalt Surface Dielectric Profiling System using Ground Penetrating Radar PP 98*. Washington, DC: American Association of State Highway and Transportation Officials.

AASHTO. 2020. *Standard Method of Test for Grain-Size Analysis of Granular Soil Materials T 311*. Washington, DC: American Association of State Highway and Transportation Officials.

AASHTO. 2022. *Standard Practice for Preparation of Cylindrical Performance Test Specimens Using the Superpave Gyratory Compactor (SGC) R 83*. Washington, DC: American Association of State Highway and Transportation Officials.

AASHTO. 2023. *Standard Method of Test for Theoretical Maximum Specific Gravity (Gmm) and Density of Hot-Mix Asphalt (HMA) T 209*. Washington, DC: American Association of State Highway and Transportation Officials.

Akay, M. F. 2009. "Support Vector Machines Combined With Feature Selection for Breast Cancer Diagnosis." *Expert Systems With Applications* 36, no. 2: 3240–3247. https://doi.org/10.1016/j.eswa.2008.01.009, last accessed March 13, 2024.

Al-Qadi, I. L., Z. Leng, S. Lahouar, and J. Baek. 2010. "In-Place Hot-Mix Asphalt Density Estimation Using Ground-Penetrating Radar." *Transportation Research Record* 2152, no. 1: 19–27. https://doi.org/10.3141/2152-03, last accessed March 13, 2024.

Araujo, S., L. Delbreilh, L. Laguerre, H. Dumont, É. Dargent, and C. Fauchard. 2016. "Rock Permittivity Characterization and Application of Electromagnetic Mixing Models for Density/Compactness Assessment of HMA by Means of Step-Frequency Radar." *Near Surface Geophysics* 14, no. 6: 551–562. https://doi.org/10.3997/1873-0604.2016031, last accessed March 13, 2024.

Aschenbrener, T., and N. Tran. 2020. "Optimizing In-Place Density Through Improved Density Specifications." *Transportation Research Record* 2674, no. 3: 211–218. https://doi.org/10.1177/0361198120908224, last accessed March 13, 2024.

ASTM. 2009. *Standard Test Method for Bulk Specific Gravity and Density of Compacted Bituminous Mixtures Using Automatic Vacuum Sealing Method D6752*. West Conshohocken, PA: ASTM International. https://10.1520/D6752-09, last accessed March 13, 2024.

ASTM. 2011. *Standard Test Method for Density of Bituminous Paving Mixtures in Place by the Electromagnetic Surface Contact Methods D2950*. West Conshohocken, PA: ASTM International. https://doi.org/10.1520/D2950, last accessed March 13, 2024.

ASTM. 2019. *Standard Guide for Using the Surface Ground Penetrating Radar Method for Subsurface Investigation D6432*. West Conshohocken, PA: ASTM International. https://www.astm.org/d6432-19.html, last accessed March 13, 2024.

Burnham, K. P., and D. R. Anderson. 2001. "Kullback-Leibler Information as a Basis for Strong Inference in Ecological Studies." *Wildlife Research* 28, no. 2: 111–119. https://doi.org/10.1071/WR99107, last accessed March 13, 2024.

Cao, Q., and I. L. Al-Qadi. 2021. "Development of a Numerical Model to Predict the Dielectric Properties of Heterogeneous Asphalt Concrete." *Sensors* 21, no. 8. https://doi.org/10.3390/s21082643, last accessed March 13, 2024.

EPA. 2023a. "Nuclear Gauges." U.S. Environmental Protection Agency. https://www.epa.gov/radtown/nuclear-gauges, last accessed March 13, 2024.

EPA. 2023b. "Dielectric Permittivity." U.S. Environmental Protection Agency. https://www.epa.gov/environmental-geophysics/dielectric-permittivity, last accessed March 13, 2024.

FHWA. 2024. *Public Roads*, Spring 2024. https://highways.dot.gov/public-roads/spring-2024/01, last accessed April 18, 2024. Washington, DC: Federal Highway Administration.

Fernandes, F. M., A. Fernandes, and J. Pais. 2017. "Assessment of the Density and Moisture Content of Asphalt Mixtures of Road Pavements." *Construction and Building Materials* 154: 1216–1225. https://doi.org/10.1016/j.conbuildmat.2017.06.119, last accessed March 14, 2024.

Hoegh, K., S. Dai, T. Steiner, and L. Khazanovich. 2018. "Enhanced Model for Continuous Dielectric-Based Asphalt Compaction Evaluation." *Transportation Research Record* 2672, no. 26: 144–154. https://doi.org/10.1177/0361198118794068, last accessed March 14, 2024.

Hoegh, K., R. Roberts, S. Dai, and E. Z. Teshale. 2019. "Toward Core-Free Pavement Compaction Evaluation: An Innovative Method Relating Asphalt Permittivity to Density." *Geosciences (Switzerland)* 9, no. 7: 1–24. https://doi.org/10.3390/geosciences9070280, last accessed March 14, 2024.

Hoegh, K., T. Steiner, E. Zegeye Teshale, and S. Dai. 2020. "Minnesota Department of Transportation Case Studies for Coreless Asphalt Pavement Compaction Assessment." *Transportation Research Record* 2674, no. 2: 291–301. https://doi.org/10.1177/0361198120907582, last accessed March 14, 2024.

Khazanovich, L., K. Hoegh, R. Conway, and S. Dai. 2017. *Non-destructive Evaluation of Bituminous Compaction Uniformity Using Rolling Density*. Washington, DC: Minnesota Department of Transportation. https://shrp2.transportation.org/documents/R06C_NonDestructiveEval.pdf, last accessed March 14, 2024.

Leng, Z. 2011. "Prediction of In-Situ Asphalt Mixture Density Using Ground Penetrating Radar: Theoretical Development and Field Verification." PhD thesis. University of Illinois at Urbana-Champaign. https://www.semanticscholar.org/paper/Prediction-of-in-situ-asphalt-mixture-density-using-Leng/c25be8c5b375944c6cdb6aa86e87925597846a38, last accessed March 14, 2024.

Leng, Z., I. L. Al-Qadi, and S. Lahouar. 2011. "Development and Validation for In Situ Asphalt Mixture Density Prediction Models." *NDT & E International* 44, no. 4: 369–375. https://doi.org/10.1016/j.ndteint.2011.03.002, last accessed March 14, 2024.

Linden, R. N., J. P. Mahoney, and N. C. Jackson. 1989. "Effect of Compaction on Asphalt Concrete Performance." *Transportation Research Record* 1217: 20–28. https://trid.trb.org/View/306988, last accessed March 14, 2024.

MnDOT. 2024a. "Continuous Asphalt Mixture Compaction Assessment Using Density Profiling System (DPS) [TPF-5(443)]." Minnesota Department of Transportation. https://www.dot.state.mn.us/materials/dps/index.html, last accessed April 18, 2024.

MnDOT. 2024b. "MnDOT Draft Field Density Profiling System Data Collection Specification." Minnesota Department of Transportation. https://edocs-public.dot.state.mn.us/edocs_public/DMResultSet/download?docId=19126991, last accessed April 8, 2024.

Nelson, S. O. 2005. "Density-Permittivity Relationships for Powdered and Granular Materials." *IEEE Transactions on Instrumentation and Measurement* 54, no. 5: 2033–2040. https://ieeexplore.ieee.org/document/1514660, last accessed March 14, 2024.

Pashoutani, S., and J. Zhu. 2020. "Ground Penetrating Radar Data Processing for Concrete Bridge Deck Evaluation." *Journal of Bridge Engineering* 25, no. 7. https://doi.org/10.1061/(asce)be.1943-5592.0001566, last accessed March 14, 2024.

Pearce, C. A. R. 1955. "The Permittivity of Two Phase Mixtures." *British Journal of Applied Physics* 6, no. 10: 358–361. https://doi.org/10.1088/0508-3443/6/10/306, last accessed March 14, 2024.

Pellinen, T., P. Eskelinen, E. Huuskonen-Snicker, and A. Hartikainen. 2015. *Assessment of Air Void Content of Asphalt Using Dielectric Constant Measurements by GPR and With VNA*. Espoo, Finland: Aalto University. https://aaltodoc.aalto.fi/items/5d1d09aa-1519-4204-801a-2c235309f60e, last accessed March 14, 2024.

Porubiaková, A., and J. Komačka. 2015. “A Comparison of Dielectric Constants of Various Asphalts Calculated From Time Intervals and Amplitudes.” *Procedia Engineering* 111: 660–665. https://doi.org/10.1016/j.proeng.2015.07.129, last accessed March 14, 2024.

Rashidi, M., and H. Azari. 2022. “On the Empirical Relationships Between the Air Content and Dielectric Constant of Hot-Mix Asphalt.” Presented at the *11th International Conference on the Bearing Capacity of Roads, Railways and Airfields*. Trondheim, Norway: Norwegian University of Science and Technology, Norwegian Public Roads Administration, Avinor, and Bane NOR. https://www.researchgate.net/publication/358930705_On_the_Empirical_Relationships_Between_the_Air_Content_and_Dielectric_Constant_of_Hot-Mix_Asphalt, last accessed March 14, 2024.

Saarenketo, T. 2013. “Measuring Electromagnetic Properties of Asphalt for Pavement Quality Control and Defect Mapping.” *Journal of Chemical Information and Modeling* 53, no. 9: 1689–1699. https://www.researchgate.net/profile/Timo-Saarenketo, last accessed March 14, 2024.

Saarenketo, T., and T. Scullion. 2000. “Road Evaluation With Ground Penetrating Radar.” *Journal of Applied Geophysics* 43, nos. 2–4: 119–138. https://doi.org/10.1016/S0926-9851(99)00052-X, last accessed March 14, 2024.

Sebesta, S., T. Saarenketo, and T. Scullion. 2012. *Using Infrared and High-Speed Ground-Penetrating Radar for Uniformity Measurements on New HMA Layers*. Washington, DC: National Academies Press. https://doi.org/10.17226/22769, last accessed March 14, 2024.

Sias, J., and E. Dave. 2023. *Laboratory Dielectric Measurement System (LDMS) for Asphalt Mixture Bulk Specific Gravity Determination*. Washington, DC: National Academies Press. https://www.trb.org/Main/Blurbs/182942.aspx, last accessed March 14, 2024.

Sihvola, A. H. 1989. “Self-Consistency Aspects of Dielectric Mixing Theories.” *IEEE Transactions on Geoscience and Remote Sensing* 27, no. 4: 403–415. https://doi.org/10.1109/36.29560, last accessed March 14, 2024.

Steiner, T., K. Hoegh, E. Z. Teshale, and S. Dai. 2020. “Method for Assessment of Modeling Quality for Asphalt Dielectric Constant to Density Calibration.” *Journal of Transportation Engineering, Part B: Pavements* 146, no. 3: 04020054. https://doi.org/10.1061/jpeodx.0000210, last accessed March 14, 2024.

Strutt, J. W. 1871. LVIII. “On the Scattering of Light by Small Particles.” *London, Edinburgh, and Dublin Philosophical Magazine and Journal of Science* 41, no. 275: 447–454. https://doi.org/10.1080/14786447108640507, last accessed March 14, 2024.

Teshale, E. Z., K. Hoegh, S. Dai, R. Giessel, and C. Turgeon. 2020. “Ground Penetrating Radar Sensitivity to Marginal Changes in Asphalt Mixture Composition.” *Journal of Testing and Evaluation* 48, no. 3: 2295–2310. https://doi.org/10.1520/JTE20190486, last accessed March 14, 2024.

Warren, C., A. Giannopoulos, and I. Giannakis. 2016. “gprMax: Open Source Software to Simulate Electromagnetic Wave propagation for Ground Penetrating Radar.” *Computer Physics Communications* 209: 163–170. https://doi.org/10.1016/j.cpc.2016.08.020, last accessed March 14, 2024.

Wilson, B., S. Sebesta, and T. Scullion. 2019. *Evaluation of the Rolling Density Meter for Rapid Continuous Measurement of Asphalt Mixture Density*. Technical Report 0-6889-R1. College Station, TX: Texas A&M Transportation Institute. https://rosap.ntl.bts.gov/view/dot/61486, last accessed March 14, 2024.

Wilson, B. T., and S. Sebesta. 2015. “Comparison of Density Tests for Thin Hot-Mix Asphalt Overlays.” *Transportation Research Record* 2504: 148–156. https://doi.org/10.3141/2504-17, last accessed March 14, 2024.

Recommended citation: Federal Highway Administration,
Validating a Density-Profiling System for Asphalt Compaction Assessment
(Washington, DC: 2024) https://doi.org/10.21949/1521588

HRDI-20/08-24(WEB)E